Comprehensive mapping of sensory and sympathetic innervation of the developing kidney

Pierre-Emmanuel Y. N'Guetta[1], Sarah R. McLarnon[1], Adrien Tassou[2], Matan Geron[2], Grégory Scherrer[3], Lori L. O'Brien[1*]

[1]Department of Cell Biology and Physiology, The University of North Carolina at Chapel Hill, Chapel Hill, NC 27599, USA

[2]Department of Cell Biology and Physiology, UNC Neuroscience Center, Department of Pharmacology, The University of North Carolina at Chapel Hill, Chapel Hill, NC 27599, USA

[3]Department of Cell Biology and Physiology, UNC Neuroscience Center, Department of Pharmacology, The University of North Carolina at Chapel Hill, Chapel Hill, NC 27599, USA; New York Stem Cell Foundation – Robertson Investigator, The University of North Carolina at Chapel Hill, Chapel Hill, NC 27599, USA

*Corresponding author: lori_obrien@med.unc.edu

Keywords: Innervation, nerve, kidney development, sympathetic, sensory

Abstract

The kidney functions as a finely tuned sensor to balance body fluid composition and filter out waste through complex coordinated mechanisms. This versatility requires tight neural control, with innervating efferent nerves playing a crucial role in regulating blood flow, glomerular filtration rate, water and sodium reabsorption, and renin release. In turn sensory afferents provide feedback to the central nervous system for the modulation of cardiovascular function. However, the cells targeted by sensory afferents and the physiological sensing mechanisms remain poorly characterized. Moreover, how the kidney is innervated during development to establish these functions remains elusive. Here, we utilized a combination of light-sheet and confocal microscopy to generate anatomical maps of kidney sensory and sympathetic nerves throughout development and resolve the establishment of functional crosstalk. Our analyses revealed that kidney innervation initiates at embryonic day (E)13.5 as the nerves associate with vascular smooth muscle cells and follow arterial differentiation. By E17.5 axonal projections associate with kidney structures such as glomeruli and tubules and the network continue to expand postnatally. These nerves are synapsin I-positive, highlighting ongoing axonogenesis and the potential for functional crosstalk. We show that sensory and sympathetic nerves innervate the kidney concomitantly and classify the sensory fibers as calcitonin gene related peptide (CGRP)$^+$, substance P$^+$, Trpv1$^+$, and Piezo2$^+$, establishing the presence of Piezo2 mechanosensory fibers in the kidney. Using retrograde tracing, we identified the primary dorsal root ganglia, T10-L2, from which Piezo2$^+$ sensory afferents project to the kidney. Taken together our findings elucidate the temporality of kidney innervation and resolve the identity of kidney sympathetic and sensory nerves.

Introduction

Major functions of the kidney include the maintenance of body fluid and electrolyte homeostasis and modulation of blood pressure. These functions are maintained by a variety of intrinsic cellular mechanisms as well as extrinsic input from the nervous system (May et al., 2010; McMahon, 2016; Osborn et al., 2021). Peripheral neurons originating from ganglia innervate the kidney and are predominantly

unmyelinated C-fibers (Kneupfer and Schramm, 1987; Booth et al., 2015; Osborn et al., 2021), although some myelinated renal afferent fibers have been reported in the kidney, yet their identity remains unclear (Simon and Schramm, 1983; Kneupfer and Schramm, 1987; Stella and Zanchetti, 1991). Kidney innervation consists of afferent sensory nerves that influence cardiovascular function through the relay of chemical and mechanical information from the kidney to the central nervous system (CNS), or efferent sympathetic nerves regulating renal function through the CNS (Osborn et al., 2021). Precise innervation and modulation of nerve activity maintains kidney physiology while aberrant nerve function is associated with several kidney diseases (DiBona & Kopp, 1997; Malpas, 2010; Sata et al., 2018). Therefore, modulating nerve activity is widely seen as a potential therapy to address kidney-related physiological disorders (Bhatt et al., 2022). Yet, to achieve such precise neuromodulation, an accurate mapping of the kidney nerve origins and a complete understanding of their molecular identity is necessary. Many studies to date have focused on sympathetic nerves and their regulation of mature kidney physiology. Therefore, we still lack detailed information about how both the sensory and sympathetic innervation of the kidney is established and how nerves pattern to reach their target cells and establish crosstalk.

Sympathetic nerves participate in the control of several kidney functions including vascular tone and glomerular filtration rate, sodium and water reabsorption, and renin release (Denton et al., 2004; DiBona, 2000; Fujisawa et al., 2011). They also modulate processes such as the release of cytokines to mediate inflammatory responses (Banek et al., 2016; Osborn et al., 2021; Veelken et al., 2008; Xiao et al., 2015). Overactivity of kidney sympathetic nerves contribute to the development and maintenance of hypertension (Osborn et al., 2021; Sata et al., 2018). In contrast to the numerous functions for sympathetic nerves in both normal physiology and pathophysiology, our understanding of kidney sensory nerve anatomy, classification, and their physiological roles remain poorly understood (Osborn et al., 2021). Kidney sensory nerves have been thus far been classified as transient receptor potential cation channel subfamily V member 1-positive (Trpv1^{+}) due to their response to capsaicin and have also been shown to produce the nociceptor-associated neuropeptides calcitonin gene-related peptide (CGRP) and substance P (Osborn et al., 2021; Tyshynsky et al., 2023).

Sensory neurons innervating the kidney project to the dorsal horn and synapse onto interneurons that project to CNS sites regulating cardiovascular function and in turn feedback to modulate kidney sympathetic nerve activity (Kopp, 2015). Recently, studies have established the importance of mechanosensitive Piezo2 sensory nerves in the urogenital system to regulate bladder and sexual function (Lam et al., 2023; Marshall et al., 2020). However, whether Piezo2 sensory nerves are also present in the kidney is unknown. Lastly, a recent study published by Cheng et. al. show parasympathetic cholinergic ($ChAT^+$ and $VAChT^+$) nerves innervate the renal artery and pelvis with cholinergic ganglion found within the kidney nerve plexus (Cheng et al., 2022). Whether these axons project to the kidney cortex and associate with cells or structures within kidney has not been elucidated to date. Initial studies of renal denervation in hypertensive patients led to a decrease in blood pressure although further intensive trials reported that certain patients experienced a rise in arterial pressure (Krum et al., 2013, 2014; Osborn & Foss, 2017; Schlaich et al., 2009; Symplicity HTN-2 Investigators et al., 2010; Townsend et al., 2017). To date, this method of controlling hypertension remains an attractive option with additional trials being conducted. However, such procedures non-selectively target both sensory and sympathetic nerves, therefore understanding the full extent of kidney nerve activity may inform efforts to optimize renal denervation strategies.

Ganglia located externally send axonal projections to the kidney. It has been reported that sympathetic innervation arises from the celiac, superior mesenteric, aorticorenal ganglia, and partially from the paravertebral chain depending on the model system being used (Barajas et al., 1992; Bell & McLachlan, 1982; Ferguson et al., 1986, 1988; Kuo et al., 1982). In rat, studies have shown that kidney sensory neurons project from dorsal root ganglion (DRG) at level T6 to L4, the majority of which derive from DRG at the level of T12–L3 (Donovan et al., 1983; Weiss & Chowdhury, 1998). However, the origin of sensory axons which innervate the mouse kidney is unclear. Moreover, the process of kidney innervation during development, in any model, has not been detailed thoroughly aside from a few recent studies reporting the close association of nerves with the developing kidney arterial tree (Honeycutt et al., 2023; Tarnick et al., 2023). In this study, we provide detailed spatiotemporal mapping of mouse kidney

sensory and sympathetic neurons across embryonic and early postnatal development, as well as their persistence in the adult. We establish when kidney innervation begins, origins in the DRG, the spatial organization and growth of axons, their association with kidney cells and structures, as well as the identity of the nerves across these different stages. Altogether, we have generated a rich resource of knowledge surrounding kidney innervation that will inform studies of both kidney development and physiological regulation.

Results

Spatiotemporal mapping of kidney innervation

Due to the lack of knowledge on how kidneys are innervated during development, we set out to determine when neuronal axons first reach the kidney and how this network subsequently expands. We generated spatiotemporal maps of kidney innervation throughout development by performing wholemount immunostaining followed by 3D light-sheet imaging of either whole urogenital systems (E12.5, E13.5) or individual kidneys (E14.5, E16.5, E18.5, P0, P7). Kidneys and urogenital systems were immunostained with the pan-neuronal marker α-tubulin class III (Tubb3, Tuj1) to visualize axons, the arterial marker α-smooth muscle actin (SMA), and the endothelial marker CD31. Our previous studies have shown that the nerves and vasculature are tightly aligned in the developing kidney, therefore we wanted to further examine the association of these two networks at the various developmental timepoints (Honeycutt et al., 2023). Male and female kidneys were both examined, with no significant differences observed. At E12.5, no Tubb3$^+$ nerves or SMA$^+$ vessels could be observed in the kidney, which was discerned by cytokeratin staining of the ureteric tree (**Fig. 1A**). SMA$^+$ cells were primarily localized to the descending aorta with no SMA$^+$ vascular mural cells yet found in the kidney, correlating with previous investigations of kidney vascularization (Daniel et al., 2018) (**Fig. 1A**). Despite the lack of axons in the kidney, we did observe the presence of ganglia and postganglionic nerve fibers tracking with the descending aorta (**Fig. 1A**). As organogenesis continues, Tubb3$^+$ nerve fibers navigate towards the kidney and begin innervation at E13.5, closely associating with SMA$^+$ mural cells which mark the maturing renal arteries (Daniel et al., 2018; Honeycutt

et al., 2023; Luo et al., 2023; Tarnick et al., 2023) (**Fig. 1B, arrowheads**). Despite the low SMA^+ vascular mural cell coverage at this timepoint, an extensive $CD31^+$ endothelial network is established in the kidney by E13.5 (**Fig. 1B**).

At E14.5, SMA coverage was more extensive, marking several arterial branches (**Fig. S1A**). Concurrently, the $Tubb3^+$ nerve fibers continue tracking with the major arterial branches, only extending along the portion of endothelium with SMA^+ vascular mural cell coverage (**Fig. S1A**). Additionally, axons track with the SMA^+ ureteric smooth muscle layer (**Fig. S1A)**. As development continues, axons grow and branch in coordination with the arterial network, highlighting a tight neurovascular interplay as the major arterial branches are established by E16.5 (**Fig. 1C**). Multiple nerve fibers associate with a single arterial branch and the larger fibers may consist of multiple axons which are tightly bundled (**Fig. 1C, arrowhead).** Once the major arterial branches were established, the axonal network expanded via interstitial branching as observed at E18.5 (**Fig. 1D**). The branching axons can be observed looping around structures such as glomeruli (**Fig. 1D, arrowhead**). Subsequent imaging of the postnatal kidney at postnatal day (P)0 (**Fig. S1B**) and P7 (**Fig. S1C**) revealed a significant increase in nerve fiber density and arborization of the network due to continued axonal growth and branching. Together, these data highlight the coordinated growth of an extensive neuronal network as kidney organogenesis progresses.

To visualize the innervation of target cells and structures within the developing kidney at greater resolution, we performed confocal imaging on E18.5 kidneys section. Supporting our wholemount 3D analyses, we observed the axons tightly associating with SMA+ vasculature, with several fibers often being associated with any one arterial branch (**Fig. 2A**). The nerves track with renal arteries and arterioles into the renal cortex and can separate from the SMA^+ vascular mural cells to loop around and associate with the Bowman's capsule of glomeruli (**Fig. 2B, Fig. 1D**) and epithelial structures (**Fig. 2C**). Overall, kidney innervation is tightly linked to arterial differentiation with axons dissociating from the SMA^+ vessels to navigate towards or around kidney target structures such as glomeruli.

Sensory nerves innervate the developing kidney

While we have mapped the spatiotemporal innervation of the developing kidney, Tubb3 is a pan-neuronal marker labeling all nerve fibers types. It is well established that the mature kidney is innervated by sympathetic neurons that modulate renal physiology, however, the contribution of sensory nerves and the timing of sensory innervation in the kidney is poorly understood (Kopp, 2015; Osborn et al., 2021). To visualize the distribution and abundance of sensory neurons in the developing kidney, we crossed a *Trpv1*^{Cre} line to the *R26*^{tdTomato} reporter line (*Trpv1*$^{Cre/+}$;*R26*$^{tdTomato/+}$) to label all nociceptive Trpv1^{+} sensory neurons. Trpv1^{+} nociceptive neurons are thought to comprise the majority of, if not all sensory nerves within the kidney and therefore labeling this population should accurately represent the sensory contribution (Stocker & Sullivan, 2023; Tyshynsky et al., 2023). We performed wholemount imaging on *Trpv1*$^{Cre/+}$;*R26*$^{tdTomato/+}$ kidneys at E16.5 to visualize the total complement of sensory nerve fibers traced from the start of kidney innervation. TdTomato^{+} signal extensively overlapped with the pan-neuronal marker Tubb3 (**Fig. 3A**). To visualize these sensory fibers and their association with kidney structures in greater detail, we examined sections from *Trpv1*$^{Cre/+}$;*R26*$^{tdTomato/+}$ kidneys at P1. The tdTomato^{+} sensory nerves are found adjacent to Lrp2^{+} proximal tubules and E-cadherin (Ecad)$^{+}$ epithelial structures (**Fig. 3B**). Additionally, sensory axons are found near arteries, arterioles, and glomeruli (**Fig. 3C**). Taken together, these findings show that sensory nerves make up a significant portion of the neuronal network in the developing kidney and associate with kidney structures by early postnatal stages.

Nociceptive sensory afferent nerve identity and function can also be defined by the production of neuropeptides such as calcitonin gene-related peptide (CGRP) and substance P. To assess renal peptidergic sensory innervation, we immunostained kidney sections at E14.5, E15.5, E18.5, P0, and adult stages using antibodies for CGRP and substance P. At E14.5 we could not yet detect CGRP^{+} or substance P^{+} nerves (**Fig. S2A, S2B**). However, by E15.5 we observed CGRP^{+} sensory nerves that closely associated with renal arteries (**Fig. 4A**). To circumvent cross-reactivity issues due to several of our antibodies being raised in the same species, we crossed the transgenic podocin Cre line (*Pod-Cre*^{tg}) to the *R26*^{tdTomato} reporter (*Pod-Cre*$^{tg/+}$;*R26*$^{tdTomato/tdTomato}$) thereby labeling all glomerular podocytes with tdTomato. Assessing kidneys from these

animals at P0, we found that CGRP$^+$ sensory nerves came in close proximity to glomeruli and proximal tubules (**Fig. 4B**). CGRP$^+$ sensory neurons were also found in adult kidneys, where they similarly associated with the vasculature and were near glomeruli (**Fig. 4C**). In contrast to CGRP, substance P immunolabelling was not detected until E18.5 where these sensory nerves were observed near blood vessels and glomeruli (**Fig. 4D**). In the adult kidneys, substance P maintained this localization pattern and was similarly found near the vasculature and glomeruli (**Fig. 4E**).

Piezo2 is a mechanoreceptor utilized by a subset of peripheral sensory neurons (Coste et al., 2010). Piezo2$^+$ neurons innervate organs of the urogenital system such as the bladder to help coordinate urination and genital sub-regions to support sexual function (Lam et al., 2023; Marshall et al., 2020). Therefore, we used immunofluorescence staining of Piezo2 on kidney sections to examine whether Piezo2$^+$ neurons also innervate the kidney during development. At E15.5, we observed Piezo2$^+$ neurons associating with the CD31$^+$ large vessels (**Fig. 4F**). By P0, we found Piezo2$^+$ neurons near glomeruli and proximal tubules (**Fig. 4G**). Collectively, our findings demonstrate the diversity of kidney sensory innervation which consists of both nociceptive and mechanosensitive neurons. The timing of when these neurons and associated neuropeptides can be detected varies throughout kidney development. However, all can be detected by birth and follow a similar pattern of association with the renal vasculature, glomeruli, and tubules.

Retrograde tracing identifies the DRG origin of kidney sensory neurons

The soma of peripheral sensory neurons are located in DRG present along the spinal column. To identify the DRG that contain the sensory neurons projecting to the kidney, we performed retrograde tracing experiments. We injected into the right kidney (ipsilateral) of adult mice the fluorescently labeled neuronal tracer Cholera toxin subunit B (CTB). Four days after the injections, both the injected and non-injected kidney as well as the ipsilateral and contralateral DRG were dissected to determine the origin of kidney sensory innervation (**Fig. 5A**). By examining the fluorescent signal from all cervical, thoracic, lumbar, and sacral DRGs, we determined that kidney sensory innervation traces to the ipsilateral DRG of the lower thoracic (T10-T13), lumbar (L1-

L6), and sacral (S1-S2) regions (**Fig. 5B**). However, the majority of sensory innervation projected from the lower thoracic (T10-T13) and upper lumber (L1-L2) regions (**Fig. 5B**). Ipsilateral kidney sections showed CTB^+ nerves near vasculature and glomeruli (**Fig. 5C**). Strikingly, we also observed CTB^+ cells within the contralateral DRG of the upper lumbar region (L1-L2), suggesting these DRG may also innervate the kidney (**Fig. 5B**). We also observed a few CTB^+ nerve fibers around blood vessels in the contralateral kidney (**Fig. 5C**). No difference was identified between male and female mice in the tracing results obtained.

Next, we specifically traced Piezo2 sensory neurons using the recombinant adeno-associated virus *pAAV-Flex-tdTomato* that we injected into the right kidney of *Piezo2*$^{EGFP\text{-}IRES\text{-}Cre/+}$ mice (**Fig. S3A**). The tracing confirmed innervation of the kidney by $Piezo2^+$ sensory neurons and shows that the majority of $Piezo2^+$ nerves project from the lower thoracic (T10-T13) and lumbar (L1 and L2) DRG (**Fig. S3B,C**). Taken together, the retrograde tracing experiments validated sensory innervation of the kidney and uncovered their origins within the lower thoracic, lumbar, and sacral regions (**Fig. 5D, S3C**). The observation that CTB^+ cells were found in L1 and L2 contralateral DRG, along with the presence of labeled axons in the contralateral kidney, suggests the possibility of cross communication between the kidneys and DRG on the opposite sides of the body.

Sympathetic and cholinergic innervation of the developing kidney

Sympathetic postganglionic neurons produce tyrosine hydroxylase (TH), an enzyme involved in catecholamine synthesis, and this marker has previously been utilized in the adult kidney to localize sympathetic nerves (Tiniakos et al., 2004; Torres et al., 2021). Thus, to determine the distribution of renal sympathetic nerves in the developing kidney we performed wholemount immunolabeling with a TH antibody at E14.5 and P0 (**Fig. 6A,B**). At E14.5, TH^+ nerve fibers were detected in the kidney, overlapping with Tubb3 and tracking with the arteries (**Fig. 6A**). By P0 the sympathetic nerves had branched significantly with the arterial tree and the axons were found navigating around structures such as $Lrp2^+$ proximal tubules (**Fig. 6B**). We also examined kidney sections and similarly observed TH^+ axons primarily associated with

renal arteries at earlier stages of development (**Fig. 6C**). By P0, the nerves could be found abutting glomeruli and proximal tubules (**Fig. 6D**). Taken together, these findings show that sympathetic neurons innervate the kidney early in development, tracking with the vasculature as they make their way to nephron targets such as tubules and glomeruli in alignment with their known physiological functions (DiBona, 2004; DiBona & Kopp, 1997; Osborn & Foss, 2017; Sata et al., 2018).

Previous studies showed that during development, TH may also be produced by cholinergic parasympathetic nerves (Howard, 2005). A recent study demonstrated parasympathetic innervation of the main renal artery and pelvis, yet there remains no anatomic evidence of significant parasympathetic innervation into the kidney. To identify whether there are cholinergic nerves in the developing kidney, we immunostained sections at E14.5, E15.5, P0, and adult for the cholinergic marker vesicular acetylcholine transporter (VAChT) (**Fig. S4**). We did not observe VAChT$^+$ nerves overlapping with pan-neuronal marker Tubb3 at E14.5 (**Fig. S4A**) even though the first nerve fibers innervating the kidney at E14.5 were TH$^+$ (**Fig. 6A**). By E15.5, we observed that Tubb3$^+$ nerves overlapped with VAChT signal, and these nerves were primarily associated with the renal artery in the kidney shown by CD31 immunostaining (**Fig. S4B**). Vascular-associated innervation increased by E16.5, and we observed VAChT$^+$ fibers around proximal tubules and glomeruli at P0 (**Fig. S4C**). In adults, the VAChT$^+$ fibers were found associated with the kidney vasculature (**Fig. S4D**). In sum, these data lend support to the presence of parasympathetic innervation into the kidney with axons reaching nephrons.

Evidence for the establishment of neuroeffector junctions during kidney development

In order to exert an impact on kidney development and physiology, neurons need to establish functional crosstalk with kidney cells. To investigate the formation of neuroeffector junctions, synapse-like structures that form between neurons and non-neuronal cells, we characterized the cellular localization of a synaptic marker by immunofluorescence on cryosectioned kidneys. Using an antibody raised against synapsin I (Syn1), a membrane-associated phosphoprotein contained within small

synaptic vesicles of presynaptic nerves, we investigated if and at which stage Syn1 is detected. At E14.5 Syn1$^+$ axons were observed around the vasculature (**Fig. 7A**). At E16.5, there was similar localization of Syn1$^+$ nerves mainly associated with the vasculature (**Fig. 7A**). By P0, Syn1$^+$ axons were localized near proximal tubules and glomeruli (**Fig. 7B**). A similar pattern was retained in the adult with Syn1$^+$ axons found along the vasculature and near glomeruli (**Fig. 7C**).

Next, we investigated the developmental expression of receptors associated with various neuronal signaling mechanisms and known post-synaptic markers to understand which kidney cells are responsive to neuronal signaling. We utilized a publicly available single cell RNA-seq dataset from the E18.5 kidney to obtain the enrichment of these factors in the various cells of the developing kidney (Combes et al., 2019) (**Fig. S5**). These data show that a variety of cell types and structures including nephron progenitors, stromal cells, renal vesicles, and the S-shaped body express α-adrenergic receptors *Adra1a* and *Adra1b*, whereas *Adra2a* and *Adra2b* were enriched in the distal tubules, ureteric epithelium, and proximal tubules (**Fig. S5A**). We also noted the β-adrenergic receptor *Adrb2* was strongly enriched in the resident immune cells while *Adrb3* was expressed by stromal cells (**Fig. S5A**). Next, we also looked for the expression of major purinergic receptors in the developing kidney. Many of the ATP and Adenosine receptors including *P2rx4, P2rx7, P2ry6, P2yr12, P2yr13, P2yr14, Lpar6,* and *Lpar4* showed enrichment in the resident immune cells. Endothelial cells, tubule epithelium, and ureteric epithelium showed expression of *Ador2a, P2ry1, Lpar6, Lpar4,* and *Adora1* while *P2rx4* and *P2ry14* were moderately enriched in podocytes (**Fig. S5B**). Lastly, we observed the enrichment of known post-synaptic markers or synapse-promoting markers like *Vamp2, Tenm3, Tenm4, Ephb1, Ephb3, Epha2, and Grm7* by podocytes, *Nlgn1, Epha2, Ephb1, and Ephb4* by endothelial cells, and *Gria3, Ephb2, Ephb3, Ephb4, Ephb6, Epha1, Epha4, Epha7, Tenm2, Dlg4, Dlg1, Nlgn3* by the distal and proximal tubules (**Fig. S5C**). Collectively, the single-cell expression data provides evidence that cells within the developing kidney express a variety of receptors and post-synaptic markers suggesting they are competent to receive and respond to neuronal-derived signals.

The spatial organization of nerves is conserved in the adult human kidney

Given the specific distribution of kidney nerves around important structures such as glomeruli and tubules in the mouse, we aimed to validate that innervation of structures in the human adult kidney was similar. First, we immunostained adult human cortex cryosections with sympathetic nerve marker TH. We observed TH^+ axons looping around glomeruli and closely associating with the Bowman's capsule similar to the mouse. These sympathetic nerves were also found near epithelial structures (ECAD+) (**Fig. 8A**). Next, we sought to confirm the presence of $PIEZO2^+$ mechanosensory afferents in the adult human kidney. We identified $PIEZO2^+$ nerves that were closely associated with glomeruli and vessels as well as the kidney epithelium (**Fig. 8B**). To validate that the nerves were actively signaling we assayed for the presence of neuroeffector junctions by immunostaining for SYN1. We observed $SYN1^+$ nerve fibers looping around glomeruli and around tubules (**Fig. 8C**). Taken together, these data show that the close association of both sympathetic and sensory nerves with vessels and nephrons is conserved in humans.

Discussion

In this study, we set out to investigate the process of kidney innervation across embryonic and postnatal mouse development. We generated spatiotemporal maps of innervation using markers specific to various classes of axons and identified the presence of both sensory and sympathetic nerves, as well as evidence for parasympathetic innervation. High resolution imaging of kidney sections provided insights into the association of nerves with kidney structures such as the vasculature, glomeruli, and tubules and the possible establishment of neuroeffector junctions. Finally, we validated that the human kidney shows similar associations of sympathetic and sensory nerve subclasses with nephron structures. Altogether, we have garnered substantial new insights into the process of kidney innervation with implications for both development and physiological regulation.

The close association of nerves with kidney vasculature

We established that kidney innervation begins at E13.5 and coincides with the initiation of arterial differentiation as vascular smooth muscle cells associate with the nascent endothelium. In the developing kidney, it has been shown that arterial differentiation is first established at E13.5 and progresses toward the kidney periphery (Daniel et al., 2018; Luo et al., 2023). Our findings of a strict association of axons with vascular smooth muscle cells correlates with a recent description of kidney innervation as well as our own recent studies (Honeycutt et al., 2023; Tarnick et al., 2023). We hypothesize that SMA+ vascular mural cells may be signaling to the axons, thereby guiding the nerves as the arteries differentiate and grow. This has been shown in other systems with axons responding to vascular-derived cues like artemin (*Artn1*) and neurotrophin 3 (*Ntf3*) (Glebova & Ginty, 2005). In the kidney, *Ntf3* is expressed by the vasculature whereas *Artn1* does not appear to be expressed, as inferred from single cell RNA-seq data of the developing kidney (Combes et al., 2019). Whether *Ntf3* or *Artn1* modulate innervation of the kidney has not been investigated to date. Once established, continued axonal growth and survival relies on neurotrophic factors such as nerve growth factor (NGF). During nephrogenesis, NGF is produced by cortical, medullary, and ureteric stroma (Combes et al., 2019; Glebova & Ginty, 2004). Additionally, it was established that NGF is required for the complete sympathetic innervation of the kidney via its interaction with its innate receptor tropomyosin receptor kinase A (TrkA) (Glebova & Ginty, 2004). Moreover, proper innervation also requires chemotactic guidance cues released by adjacent cells within the tissue. In the kidney, we and others have established that proper patterning of the neurovascular network is mediated by the guidance cue netrin-1 (Honeycutt et al., 2023; Luo et al., 2023). However, we established that the endothelium is the primary responder to netrin-1 guidance cues, with the nerves following the vascular pattern, suggesting the SMA^+ vascular mural cells themselves play a significant role in guiding kidney innervation (Honeycutt et al., 2023). While it has been established that netrin-1 plays a key role in synapse formation and axonal regeneration in the brain, we do not know whether the same is true in the kidney (Zheng et al., 2018). Additional studies are necessary to establish the full complement of cues necessary for proper kidney innervation and the establishment of functional crosstalk.

The diversity of kidney nerves

During kidney development, we found that both sensory and sympathetic nerves innervate the tissue early in development and branch following the arterial tree. Sensory nerves could be classified as nociceptive by Trpv1$^+$ lineage tracing. The limitation of this approach is that as neurons mature, they may not remain Trpv1$^+$. As such, and with the lack of our ability to identify a Trpv1 antibody that worked on our kidneys, this lineage trace only serves as a proxy for Trpv1$^+$ nerves that innervate the kidney from the onset. However, we were able to further classify the sensory neurons by their production of the neuropeptides CGRP and substance P. CGRP$^+$ nerves were identified earlier in development than substance P$^+$ nerves (E15.5 vs. E18.5), but both did not appear until innervation had already been established for several days. With the importance of neurotrophic factors for proper sensory afferent nerve function, these delays in production could be due to changes in molecular cues required for their specific growth and function (Ernsberger et al., 2020; Golden et al., 2010). The expression of their innate target receptor on kidney cells could also play an important role in triggering neuropeptide production. Despite these differences, all the sensory nerve markers showed similar tracking with the vasculature and association with kidney target structures such as glomeruli and tubules around E18.5 to P0.

Recent studies have established the expression of the *Piezo2* mechanosensory receptor by stromal progenitor cells during kidney development, as well as juxtaglomerular (JG) cells and glomerular mesangial cells in the adult kidney (Mochida et al., 2022, Hill et al., 2023). While our antibody labeling did not detect these Piezo2$^+$ cells, this was also noted in the study by Mochida et al. where RNAScope *in situ* hybridization was necessary to detect *Piezo2* expression. We have established the presence of Piezo2/PIEZO2$^+$ sensory nerves in both the mouse and human kidney where they associate with the vasculature, glomeruli, and proximal tubules. We hypothesize that these sensory axons are poised to sense changes in pressure or volume within the kidney. It has been established that Piezo2$^+$ cells in the bladder communicate with pressure sensitive Piezo2$^+$ afferent nerves to mediate micturition (Marshall et al., 2020), and Piezo2 signaling is critical for sexual function (Lam et al.,

2023). Intriguingly, a recent report suggests that Piezo2 in JG cells modulates renin levels (Hill et al., 2023). However, further investigation is required to understand whether such communication between Piezo2$^+$ kidney cells and Piezo2$^+$ sensory neurons play a role in development or physiological function. Interestingly, many of these sensory nerves are seen looping in a “hairpin” fashion around glomeruli and tubules. Such anatomic position may better enable the ability to sense changes in pressure, volume, filtration rate, and tubule physiology ensuring homeostatic control. The looping may also enable innervation of structures within the kidney without the need for a singular synapse to each kidney cell. These findings further emphasize the need for studies investigating the physiological role of sensory afferent nerves in the control of kidney development and function in health and disease.

In addition to the sensory nerves, we also showed that TH$^+$ sympathetic efferent nerves innervate the developing kidney. TH$^+$ axons were detected as early as E14.5 and as development progressed, TH$^+$ nerves associated with the vasculature, tubules, and glomeruli. Association with these structures correlates with the known physiological functions of sympathetic nerves in modulating vascular tone, tubular sodium reabsorption, and renin release by JG cells (Osborn et al., 2021; Osborn & Foss, 2017). It has been established that renal sympathetic nerves contribute to the pathogenesis of hypertension. Thus, procedures like catheter-based renal denervation are seen as novel therapies that could reduce blood pressure in hypertensive patients (Esler et al., 2012; Krum et al., 2013, 2014). However, this procedure non-selectively targets all renal nerves and a deeper understanding of the interplay between sympathetic and sensory nerves in the mediation of physiology may inform efforts to optimize these ablation strategies.

Most visceral organs are innervated by both sympathetic and parasympathetic nerves. This is no exception to the kidney which was first hypothesized to harbor parasympathetic nerves that enter the kidney along the renal vasculature (Mitchell, 1950). Yet, there remains no significant anatomic evidence of extensive parasympathetic innervation within the kidney, and this remains a topic of debate. In our study, we observed Tubb3$^+$ nerve fibers which colocalized with the cholinergic marker VAChT. However, this could represent a subset of immature sympathetic nerves

expressing both VAChT and TH, although as development progressed, we observed VAChT$^+$ nerves in the cortex associating with structures such as tubules which are more likely to represent mature, functional parasympathetic nerves. Higher resolution imaging studies are needed to determine if these are sympathetic nerves expressing cholinergic markers or whether they represent separate classes. Recently, research by Cheng et al. on adult mouse renal arteries showed the presence of periarterial cholinergic nerves which were separate from sympathetic and sensory nerve fibers (Cheng et al., 2022). Together, these findings point to the potential for greater contribution of parasympathetic activity in the modulation or kidney function than has been previously appreciated, although further characterization is necessary.

Common DRG projections to organs of the urogenital system

The regulation of kidney homeostasis is in part maintained by neuronal modulation. Ablation of renal nerve activity is widely seen as a way to treat diseases like hypertension. Accurate mapping and understanding the molecular identity of kidney nerves will help guide such interventions. However, studies have largely focused on kidney sympathetic nerves and only recently has the contribution of sensory neurons to physiological regulation been more thoroughly investigated (Banek et al., 2016; Ong et al., 2019; Osborn et al., 2021). Building on these previous studies, we found that kidney sensory innervation is substantial and molecularly diverse. Axons from sensory neurons form an extensive network in the developing kidney that continues to expand with maturation. Validation of sensory innervation was provided by retrograde tracing and identified the DRG origins of these nerves. Kidney sensory innervation primarily traces to the lower thoracic region from DRG T10-T13, the lumbar region from DRG L1-L6, and the sacral region from DRG S1 and S2. However, the DRG labeling was variable with the majority of axons innervating the kidney projecting from T10-13 and L1-L2. Piezo2$^+$ neurons similarly traced to the DRG at these levels. Tracing performed in the mouse bladder and prostate via the application of FastBlue dye revealed similar projection of neurons from T13, L1, L2, L6, and S1 (Lee et al., 2016). This suggests that organs of the genitourinary system are largely innervated from common DRG. Interestingly, our CTB tracing experiment also showed that contralateral DRG at L1 and

L2 were positive for CTB. These data suggest that some axons innervating the kidney might originate from contralateral DRG or that the same DRG in the ipsilateral side sends axons to both kidneys. Concurrent retrograde labeling of sensory nerves in the bladder and colon showed that dichotomizing afferent nerves coming from an individual DRG neuron innervate both the colon and the bladder (Christianson et al., 2007). Such connectivity is important for integrating sensory input from multiple organs and likely plays a major role in pelvic pain disorders.

Establishing crosstalk during kidney development

During development the nerves lie in close association with the vasculature, tubules, and glomeruli suggesting potential functional crosstalk. Sympathetic and sensory nerves branch with the vasculature and dissociate to navigate through the tissue where they appear to loop around glomeruli and come in close proximity to tubules. Such close association likely allows for the formation of neuroeffector junctions with target structures and allow nerves to functionally innervate multiple structures as axons navigate around them. As reviewed previously (Barajas et al., 1984; DiBona & Kopp, 1997; Osborn et al., 2021), these fiber varicosities could impact adjacent kidney cells by establishing neuroeffector junctions more than 50μm away from the neurotransmitter release site, allowing for diffusion throughout the interstitium and to target cells. To investigate the presence of neuroeffector junctions in the kidney, we assessed the localization of synapsin I, which is a major component of pre-synaptic vesicles and important for axonogenesis (Chin et al., 1995). Early during development, we observed that synapsin I is mainly localized near vasculature and this localization profile is extended to the glomeruli and tubule by E18.5. Such findings agree with our current understanding of kidney development and physiology. Mouse kidney development continues postnatally contrary to human kidney development which is finished before birth (McMahon, 2016). We also know that the mouse kidney forms around 90% of its nephrons towards the end of ureteric branching with 40% of them differentiating after birth (Smyth, 2021). Yet, kidney function must be established very early on in newborn pups. Thus, it is likely important to establish proper innervation of the developing kidney to regulate homeostasis. Interestingly, data mining through

publicly available single cell RNA-seq datasets of E18.5 kidneys (Combes et al., 2019) suggests that many AMPA (*Gria1*, *Gria3*, *Gria4*) and NMDA (*Grin3a*) receptors are expressed by different nephron and stromal progenitors, as well as early proximal tubules. While it has been established that glutamatergic signaling via NMDA maintains the epithelial phenotype of proximal tubular cells through calcium signaling in a proximal tubule cell line (HK-2) (Bozic et al., 2011), it remains unclear what role glutamate transport may play in the proper development of proximal tubules. Overall, the expression of neurotransmitter receptors and postsynaptic markers in the developing kidney suggests the potential for several neuronal signaling mechanisms that regulate development and function.

Limitations of our studies

To our knowledge, our study is the first to provide a thorough characterization of kidney innervation detailing the spatial and temporal establishment of nerve networks during development, including association and putative crosstalk with target structures. Importantly, we establish that a significant portion of the nerve network consists of sensory afferent axons with the novel identification of Piezo2^{+} mechanosensory neurons. However, it is important to note some assumptions which guided our study. For the classification of noradrenergic sympathetic nerves, we use TH as a marker. The strong expression of TH by sympathetic ganglion near the descending aorta support our finding that TH^{+} sympathetic nerves are abundant in the kidney. However, some TH^{+} axons in the developing kidney may project from the DRG (Meerschaert et al., 2020) thus we cannot omit that a certain percentage of these nerves may be sensory, although this is likely to be a minor percentage given the low level of TH expression within sensory ganglia prior to birth (Smith-Anttila et al., 2021). Finally, we relied on the careful study of technical and biological replicates but did not quantify axon metrics such as density or percent of sympathetic versus sensory nerves. Hence, there is a possibility that we did not identify more subtle differences among stages and classes of nerves, in addition to sex differences. Future investigations are necessary to parse out these details and to also determine the significance of these nerves to overall kidney development and the establishment of proper function.

Materials and methods

Animals

All procedures and experiments were performed according to the guidelines of the National Institutes of Health Guide for the Care and Use of Laboratory Animals and were approved by the Institutional Animal Care and Use Committees of The University of North Carolina at Chapel Hill protocols 19-183 and 22-136. Mice were grouped and housed in a 12-h light-dark cycle with ad libitum access to food and water. Adult Swiss Webster (Taconic stock: SW MPF) and C57Bl6/J (Jackson Labs/JAX stock #: 000664) mice were purchased from the respective vendor for in house matings. Swiss Webster incrosses were utilized for all experiments involving only wild type mice. C57Bl/6J mice were utilized for maintenance of transgenic and knock-in lines. *Trpv1*^{Cre} (JAX stock #:017769)(Cavanaugh et al., 2011) were maintained as a homozygous line, *Pod-Cre*^{tg} mice (JAX stock #:008205)(Moeller et al., 2003) were maintained as heterozygotes, *R26*^{tdTomato} (JAX stock #:007914)(Madisen et al., 2010) mice were maintained as a homozygous line, and *Piezo2*$^{EGFP\text{-}IRES\text{-}Cre}$ (JAX stock #:027719) (Woo et al., 2014) mice were maintained as heterozygotes.

Tissue collection and processing

For all mouse experiments, mattings were set up in the afternoon and copulation plugs found the following day were designated as embryonic day (E)0.5. The day of birth was considered postnatal day (P)0. This occurred at E19.5, births earlier or later than E19.5 were not utilized in these studies. At the desired developmental time point, pregnant dams were sacrificed by CO_2 inhalation, and death was confirmed by cervical dislocation. Mouse embryos were excised from the uterus and kidneys or whole urogenital systems dissected in ice-cold 1x phosphate-buffered saline (PBS). For genetic crosses, tail or ear clips were taken and incubated with DirectPCR lysis buffer (Viagen Biotech; Cat#102-T) containing 10µg/mL proteinase K (Sigma; Cat#3115836001), incubated at 55°C overnight, and denatured at 95°C for 20 min the next day. Genotyping was performed using JAX genotyping protocols and recommended primers with the following PCR parameters: annealing temperature T_{anl} =

58°C, elongation time t_{elg} = 40 sec for 35 cycles. To ensure biological significance, we analyzed a minimum of 3 animals per neuronal marker for both sexes at the following stages: E12.5, E13.5, E14.5, E16.5, E18.5, P0, P7, and adults (6-10 weeks old). For tissue processing, all steps below were performed on rotating shakers. Harvested kidneys or urogenital systems from embryonic and postnatal mice were fixed by immersion in fresh ice-cold 4% PFA-PBS (Fishersci, Cat#15714) at 4°C for 30 min, while kidneys obtained from juvenile and adult mice were fixed by immersion in fresh ice-cold 4% PFA-PBS at 4°C for 2 hours. Next, all kidneys were washed in ice-cold 1x PBS three times for 10 min each at room temperature and stored at 4°C in 1x PBS until use. All kidneys destined to be sectioned were incubated in ice-cold 30% sucrose-PBS solution overnight. The next day, kidneys were then embedded in Tissue freezing media (Fishersci, Cat#23730571) and sectioned at 12µm on a Leica cryostat CM1850. Slides were stored at -80°C until use.

Human kidney tissue samples were obtained from the UNC Tissue Procurement Facility and were de-identified and therefore were exempt from IRB approval. Tissue was obtained as a frozen block. A small piece of tissue was removed with a razor blade, fixed for 10 min in 4% paraformaldehyde, and subsequent processing for cryosectioning and immunofluorescence was carried out as for the mouse.

Cholera Toxin B(CTB) and pAAV-FLEX-tdTomato retrograde tracing

Surgeries were performed as in Woodard et al., 2018. Briefly, mice were anesthetized with isoflurane inhalation and the right kidney accessed via flank incision. The kidney was exposed and carefully isolated with cotton-tip applicators from peripheral fat or connective tissues in order to not disrupt nerve connections. For retrograde labeling of the DRGs innervating the kidney, 4 injections of 3µl 0.2% CTB-555 were administered to 4 males and 4 females on a C57Bl6/J and Swiss Webster background. For retrograde labeling of the Piezo2^{+} nerves innervating the kidney, 4 injections of 5µl of *pAAV-FLEX-tdTomato* (plamid #28306) were administered to 2 males and 2 females *Piezo2*$^{EGFP\text{-}IRES\text{-}Cre/+}$ (Jax# 027719). All injections were administered directly into kidney tissue through the renal capsule. The 4 injections consisted of one cortical injection per pole of the kidney, one injection in the medulla,

and one injection in the renal pelvis. For each injection, the needle was left inside the tissue after injection for an additional 1 minute to avoid back-leak. After injections, the muscle and skin were closed with sutures, and bupivacaine was administered for analgesia. After suturing, mice were housed in a clean cage with heat pads underneath until ambulatory. Mice were euthanized 4 days after CTB injections and 4 weeks after *pAAV-FLEX-tdTomato* injections. Mice were perfused with 30ml 1x PBS and 20ml 4%PFA-PBS with kidneys and DRGs collected for tissue sectioning and imaging.

Section immunofluorescence

Kidney sections for immunofluorescence were removed from the -80°C freezer and allowed to equilibrate to room temperature for 10 min. Sections were rehydrated, and the freezing medium was removed by incubating the slide in 1x PBS for 10 min in a Coplin jar. After rehydration, excess PBS was removed from the slide then a hydrophobic barrier was drawn around the section using a hydrophobic pap pen (Vector Laboratories, Cat#H-4000). Sections were incubated for 30 min in blocking solution (ice-cold PBS solution with 4% donkey serum (Equitech-Bio, Cat#SD30-0100), 1% bovine serum albumin (Fishersci, Cat#BP9706-100), and 0.25% Triton X-100 (Fishersci, Cat#BP151-500). Slides were then incubated at room temperature for 2 hours covered from light with primary antibodies in block solution (see Supplemental Table 1 for primary antibodies utilized; Piezo2 antibodies were combined as a mixture for detection). After primary incubation, slides were washed 3 times for 5 min at room temperature covered from light with wash solution (PBS + 0.25% Triton X-100) before incubating them for 45 min at room temperature covered from light with the appropriate Alexa Fluor secondary antibody (488, 568, or 647 conjugated; ThermoFisher) in blocking solution. Finally, slides were washed 4 times for 5min at room temperature covered from light using wash solution with the last wash containing DAPI diluted at 1:10000. Slides were mounted using Prolong gold mounting media (ThermoFisher, Cat#P36930), and images were captured with a Zeiss 880 confocal laser scanning microscope.

Wholemount immunofluorescence and tissue clearing

For mouse embryonic and postnatal kidneys or urogenital systems (E12.5-P7), we used a modified version of the original iDISCO protocol (Renier et al., 2014) for wholemount immunolabelling (see Supplemental Table 2) using validated antibodies and concentrations indicated in Supplemental Table 1. All steps are performed on rotating shakers. We first incubated whole pre-fixed tissue in 1ml blocking solution (ice-cold PBS solution with 10% (v/v) Heat Inactivated Sheep Serum (HISS) (ThermoFisher, Cat# 16070096) and 0.5% (v/v) Triton X-100) for 1hr at room temperature. Then, we incubated the blocked kidney in 1ml primary antibody in block solution for 7 days at 4°C while covered from light. The labeled kidney was then washed using 1ml wash buffer (PBS solution with 0.25% Triton X-100) for a whole day at room temperature covered from light with wash solution changed every 1 hour. After washing, labeled kidneys were incubated in 1ml secondary antibody in block solution at a concentration of 1:1000 for 3.5 days at 4°C while covered from light. After secondary antibody labeling, kidneys were washed again using 1ml wash buffer for a whole day at room temperature covered from light with wash solution changed every 1 hour. Before optical clearing, successful labeling was checked on a widefield Leica fluorescent microscope (Leica DMi8). Labeled kidneys were then embedded in 1% agarose (Fishersci, Cat#BP160-500) gel made with 1x TAE, the agarose block was cut to a size of 5mmx5mm to ensure proper mounting on the light-sheet microscope. To clear kidneys, we first dehydrated the agarose block in a methanol-H_20 (Fishersci, Cat#A433P-4) series wash at room temperature (25%, 50%, 75%, and 100%) for 1 hour each minimum covered from light. Next, dehydrated agarose blocks were incubated in 66% v/v dichloromethane (DCM) (Sigma, Cat#270997-2L)/33% v/v methanol for 3 hours at room temperature covered from light. Following this, the agarose blocks were then incubated in 100% DCM for 15min x 2 at room temperature covered from light. Finally, the fully dehydrated agarose blocks were incubated in 100% v/v dibenzyl ether (DBE) (Sigma, Cat#33630-1L) and stored at room temperature away from light. The blocks became transparent and invisible within 5-7hr and were stored in DBE until imaging. The DBE was changed out for fresh DBE before imaging the sample.

3D light-sheet and confocal imaging

All whole-mount images were obtained using the LaVision BioTec Ultramicroscope II light-sheet system at the UNC Microscopy Services Laboratory (MSL). This light-sheet is outfitted with an Andor Zyla 5.5 sCMOS detector, an Olympus MVPLAPO 2X/0.5 objective coupled to a zoom body ranging from 1.26x to 12.6x with a corrected dipping cap and a working distance of 5.7mm. All whole-mount images in this study were imaged with laser wavelengths: 488, 561, and 647nm as well as 3 angled light-sheet from one side only with the following parameters: sheet NA of 0.016, horizontal focus set in the middle of the sample, correction collar set at 3.5 and 2µm Z-spacing (step size). All tiff images are generated in 16-bit. All confocal images were obtained using a Zeiss 880 confocal laser scanning microscope in the UNC Hooker Imaging Core via the Zen 2 software with 34-channel gallium arsenide phosphide (GaAsP) detectors. All images obtained were imaged using a Plan-Neofluar 40x/NA:1.3 or 63x/NA:1.4 oil objective with the following working distance respectively: 0.21mm and 0.19mm. Pinhole size of 1AU set on the longest wavelength fluorophore with the same diameter size for all the rest. All image acquisition settings can be found in Supplemental Table 3.

Image processing

Images, 3D volume, and movies were generated using Imaris x64 software version 9.9.1. All stack images obtained from light-sheet imaging were first converted into an imaris file (.ims) using Imaris File Converter version 9.8.2. All wholemount images and videos were obtained using the “snapshot” and “animation” tools in Imaris 9.9.1. files obtained from Zeiss confocal microscope (.czi) were converted into an Imaris file using Imaris File Converter 9.8.2. Tilescan images were stitched with 20% overlapped using Imaris stitcher 9.9.1 and image analysis was done in Imaris version 9.9.1.

Receptor and postsynaptic marker scRNA-seq enrichment

To identify the kidney cell populations in which nerve associated receptors and markers were expressed, the selected genes were analyzed for their relative enrichment within the single cell RNA-seq data from E18.5 kidneys (Combes et al.,

2019). Heatmaps were generated in R (R Core Team, 2021) using the ggplot2 package (Wickham, 2009) and ComplexHeatmap (Gu et al. 2016). Log fold change values were obtained from Combes et al., 2019 Table S1 "lookup" tab.

Acknowledgments

We thank members of the O'Brien Lab for their critical insights throughout the project. We would like to thank Dr. Pablo Ariel director of the UNC Microscopy Services Laboratory for expert training in light-sheet image acquisition and analysis and lending his expertise throughout the project, and Dr. Wendy Salmon director of the UNC Hooker Imaging Core for confocal microscopy imaging training. The Microscopy Services Laboratory in the Department of Pathology and Laboratory Medicine and the Department of Cell Biology and Physiology Hooker Imaging Core are supported by the NIH P30CA016086 Cancer Center Core Support Grant to the UNC Lineberger Comprehensive Cancer Center. Light-sheet microscopy at MSL is also supported in part by the North Carolina Biotech Center Institutional Support Grant 2016-IDG-1016, and Andor Dragonfly microscope was funded with support from National Institutes of Health grant S10OD030223.

Conflict of Interest

The authors declare that they have no conflict of interest

Funding

This work was supported by NIH R01DK121014 to L.L.O, NIH R01DA044481 and W81XWH-15-1-0076 Neurosensory Research Award from the Department of Defense to G.S., and a Helen Lyng White postdoctoral fellowship to A.T. G.S. is a New York Stem Cell Foundation – Robertson Investigator.

Authors Contributions

L.L.O. conceptualized the study, supervised research, guided experiments, interpreted data, and revised the manuscript. P-E.Y.N. performed experiments, data analysis, interpreted data, and wrote the manuscript. S.R.M. performed mouse surgery

required for retrograde tracing and helped with Piezo2 analysis. P-E.Y.N. and A.T. injected mice for retrograde tracing experiment. A.T. and M.G. dissected, imaged and analyzed DRGs data. All authors contributed to the manuscript text. G.S. interpreted retrograde tracing data and supervised A.T. and M.G. research.

References

Banek, C. T., Knuepfer, M. M., Foss, J. D., Fiege, J. K., Asirvatham-Jeyaraj, N., Van Helden, D., Shimizu, Y., & Osborn, J. W. (2016). Resting Afferent Renal Nerve Discharge and Renal Inflammation. *Hypertension*, *68*(6), 1415-1423. https://doi.org/10.1161/hypertensionaha.116.07850

Barajas, L., Liu, L., & Powers, K. (1992). Anatomy of the renal innervation: intrarenal aspects and ganglia of origin. *Can J Physiol Pharmacol*, *70*(5), 735-749. https://doi.org/10.1139/y92-098

Barajas, L., Powers, K., & Wang, P. (1984). Innervation of the renal cortical tubules: a quantitative study. *Am J Physiol*, *247*(1 Pt 2), F50-60. https://doi.org/10.1152/ajprenal.1984.247.1.F50

Bell, C., & McLachlan, E. M. (1982). Dopaminergic neurons in sympathetic ganglia of the dog. *Proceedings of the Royal Society of London. Series B. Biological Sciences*, *215*(1199), 175-190. https://doi.org/10.1098/rspb.1982.0036

Bhatt, D. L., Vaduganathan, M., Kandzari, D. E., Leon, M. B., Rocha-Singh, K., Townsend, R. R., Katzen, B. T., Oparil, S., Brar, S., DeBruin, V., Fahy, M., Bakris, G. L., & Investigators, S. H.-S. C. (2022). Long-term outcomes after catheter-based renal artery denervation for resistant hypertension: final follow-up of the randomised SYMPLICITY HTN-3 Trial. *Lancet*, *400*(10361), 1405-1416. https://doi.org/10.1016/S0140-6736(22)01787-1

Bozic, M., de Rooij, J., Parisi, E., Ortega, M. R., Fernandez, E., & Valdivielso, J. M. (2011). Glutamatergic signaling maintains the epithelial phenotype of proximal tubular cells. *J Am Soc Nephrol*, *22*(6), 1099-1111. https://doi.org/10.1681/ASN.2010070701

781 Brading, A. (1999). *The autonomic nervous system and its effectors*. Blackwell Science.
782 Booth LC, May CN, Yao ST. The role of the renal afferent and efferent nerve fibers in heart
783 failure. Front Physiol. 2015 Oct 1;6:270. doi: 10.3389/fphys.2015.00270.
784 Cheng, X., Zhang, Y., Chen, R., Qian, S., Lv, H., Liu, X., & Zeng, S. (2022). Anatomical Evidence for
785 Parasympathetic Innervation of the Renal Vasculature and Pelvis. *J Am Soc Nephrol*,
786 *33*(12), 2194-2210. https://doi.org/10.1681/ASN.2021111518
787 Chin, L. S., et al. (1995). "Impairment of axonal development and of synaptogenesis in
788 hippocampal neurons of synapsin I-deficient mice." Proc Natl Acad Sci U S A 92(20):
789 9230-9234.
790 Christianson, J. A., Liang, R., Ustinova, E. E., Davis, B. M., Fraser, M. O., & Pezzone, M. A. (2007).
791 Convergence of bladder and colon sensory innervation occurs at the primary afferent
792 level. *Pain*, *128*(3), 235-243. https://doi.org/10.1016/j.pain.2006.09.023
793 Combes, A. N., Phipson, B., Lawlor, K. T., Dorison, A., Patrick, R., Zappia, L., Harvey, R. P.,
794 Oshlack, A., & Little, M. H. (2019). Single cell analysis of the developing mouse kidney
795 provides deeper insight into marker gene expression and ligand-receptor crosstalk.
796 *Development*, *146*(12), dev178673. https://doi.org/10.1242/dev.178673
797 Coste, B., et al. (2010). "Piezo1 and Piezo2 are essential components of distinct mechanically
798 activated cation channels." Science 330(6000): 55-60.
799 Daniel, E., Azizoglu, D. B., Ryan, A. R., Walji, T. A., Chaney, C. P., Sutton, G. I., Carroll, T. J.,
800 Marciano, D. K., & Cleaver, O. (2018). Spatiotemporal heterogeneity and patterning of
801 developing renal blood vessels. *Angiogenesis*, *21*(3), 617-634.
802 https://doi.org/10.1007/s10456-018-9612-y
803 Denton, K. M., Luff, S. E., Shweta, A., & Anderson, W. P. (2004). DIFFERENTIAL NEURAL
804 CONTROL OF GLOMERULAR ULTRAFILTRATION. *Clinical and Experimental Pharmacology*
805 *and Physiology*, *31*(5-6), 380-386. https://doi.org/10.1111/j.1440-1681.2004.04002.x
806 Dibona, G. F. (2000). Nervous Kidney. *Hypertension*, *36*(6), 1083-1088.
807 https://doi.org/10.1161/01.hyp.36.6.1083
808 DiBona, G. F., & Kopp, U. C. (1997). Neural control of renal function. *Physiol Rev*, *77*(1), 75-197.
809 https://doi.org/10.1152/physrev.1997.77.1.75
810 DiBona, G. F. (2004). "The sympathetic nervous system and hypertension: recent
811 developments." Hypertension 43(2): 147-150.
812 Donovan, M. K., Wyss, J. M., & Winternitz, S. R. (1983). Localization of renal sensory neurons
813 using the fluorescent dye technique. *Brain Res*, *259*(1), 119-122.
814 https://doi.org/10.1016/0006-8993(83)91072-7
815 Ernsberger, U., Deller, T., & Rohrer, H. (2020). The diversity of neuronal phenotypes in rodent
816 and human autonomic ganglia. *Cell Tissue Res*, *382*(2), 201-231.
817 https://doi.org/10.1007/s00441-020-03279-6
818 Esler, M. D., Krum, H., Schlaich, M., Schmieder, R. E., Bohm, M., Sobotka, P. A., & Symplicity, H.
819 T. N. I. (2012). Renal sympathetic denervation for treatment of drug-resistant
820 hypertension: one-year results from the Symplicity HTN-2 randomized, controlled trial.
821 *Circulation*, *126*(25), 2976-2982. https://doi.org/10.1161/CIRCULATIONAHA.112.130880
822 Ferguson, M., Ryan, G. B., & Bell, C. (1986). Localization of sympathetic and sensory neurons
823 innervating the rat kidney. *Journal of the Autonomic Nervous System*, *16*(4), 279-288.
824 https://doi.org/10.1016/0165-1838(86)90034-2

825 Ferguson, M., Ryan, G. B., & Bell, C. (1988). The innervation of the renal cortex in the dog. *Cell*
826 *and Tissue Research*, *253*(3). https://doi.org/10.1007/bf00219744
827 Fujisawa, Y., Nagai, Y., Lei, B., Nakano, D., Fukui, T., Hitomi, H., Mori, H., Masaki, T., &
828 Nishiyama, A. (2011). Roles of central renin-angiotensin system and afferent renal nerve
829 in the control of systemic hemodynamics in rats. *Hypertension Research*, *34*(11), 1228-
830 1232. https://doi.org/10.1038/hr.2011.115
831 Ginty, N. O. G. a. D. D. (2004). Heterogeneous Requirement of NGF for Sympathetic Target
832 Innervation In Vivo. *Journal of Neuroscience*, *24*(3), 743-751.
833 https://doi.org/10.1523/jneurosci.4523-03.2004
834 Glebova, N. O., & Ginty, D. D. (2005). GROWTH AND SURVIVAL SIGNALS CONTROLLING
835 SYMPATHETIC NERVOUS SYSTEM DEVELOPMENT. *Annual Review of Neuroscience*, *28*(1),
836 191-222. https://doi.org/10.1146/annurev.neuro.28.061604.135659
837 Golden, J. P., Hoshi, M., Nassar, M. A., Enomoto, H., Wood, J. N., Milbrandt, J., Gereau, R. W. t.,
838 Johnson, E. M., Jr., & Jain, S. (2010). RET signaling is required for survival and normal
839 function of nonpeptidergic nociceptors. *J Neurosci*, *30*(11), 3983-3994.
840 https://doi.org/10.1523/JNEUROSCI.5930-09.2010
841 Gu, Z., et al. (2016). "Complex heatmaps reveal patterns and correlations in multidimensional
842 genomic data." Bioinformatics 32(18): 2847-2849.
843 Hill, R.Z., Shirvan, S., Burquez, S., Dubin, A.E., Servin-Vences, M.R., Miner, J.H., & Patapoutian,
844 A. (2023). Renal mechanotransduction is an essential regulator of renin. *bioRxiv,*
845 2023.11.04.565646; doi: https://doi.org/10.1101/2023.11.04.565646.
846 Howard, M. J. (2005). Mechanisms and perspectives on differentiation of autonomic neurons.
847 *Dev Biol*, *277*(2), 271-286. https://doi.org/10.1016/j.ydbio.2004.09.034
848 Honeycutt, S. E., N'Guetta, P.Y., Hardesty, D.M., Xiong, Y., Cooper, S.L., Stevenson, M.J., &
849 O'Brien, L.L. (2023). Netrin-1 directs vascular patterning and maturity in the developing
850 kidney. *Development*. doi: 10.1242/dev.201886. PMID: 37818607
851 Kopp, U. C. (2015). Role of renal sensory nerves in physiological and pathophysiological
852 conditions. *Am J Physiol Regul Integr Comp Physiol*, *308*(2), R79-95.
853 https://doi.org/10.1152/ajpregu.00351.2014
854 Krum, H., Schlaich, M., & Sobotka, P. (2013). Renal Sympathetic Nerve Ablation for Treatment-
855 Resistant Hypertension. *British Journal of Clinical Pharmacology*, n/a-n/a.
856 https://doi.org/10.1111/bcp.12171
857 Krum, H., Schlaich, M. P., Sobotka, P. A., Bohm, M., Mahfoud, F., Rocha-Singh, K., Katholi, R., &
858 Esler, M. D. (2014). Percutaneous renal denervation in patients with treatment-resistant
859 hypertension: final 3-year report of the Symplicity HTN-1 study. *Lancet*, *383*(9917), 622-
860 629. https://doi.org/10.1016/S0140-6736(13)62192-3
861 Kuo, D. C., de Groat, W. C., & Nadelhaft, I. (1982). Origin of sympathetic efferent axons in the
862 renal nerves of the cat. *Neurosci Lett*, *29*(3), 213-218. https://doi.org/10.1016/0304-
863 3940(82)90319-6
864 Knuepfer M, Schramm LP. The conduction velocities and spinal projections of single renal
865 afferent fibers in the rat. Brain Res 435: pp. 167–73, 1987. 10.1016/0006-
866 8993(87)91598-8.

867 Lee, S., Yang, G., Xiang, W., & Bushman, W. (2016). Retrograde double-labeling demonstrates
868 convergent afferent innervation of the prostate and bladder. *Prostate*, *76*(8), 767-775.
869 https://doi.org/10.1002/pros.23170
870 Lam, R. M., et al. (2023). "PIEZO2 and perineal mechanosensation are essential for sexual
871 function." Science 381(6660): 906-910.
872 Luo, P. M., et al. (2023). "Stromal netrin-1 coordinates renal arteriogenesis and mural cell
873 differentiation." Development.
874 Malpas, S. C. (2010). Sympathetic nervous system overactivity and its role in the development
875 of cardiovascular disease. *Physiol Rev*, *90*(2), 513-557.
876 https://doi.org/10.1152/physrev.00007.2009
877 May, C. N., Frithiof, R., Hood, S. G., McAllen, R. M., McKinley, M. J., & Ramchandra, R. (2010).
878 Specific control of sympathetic nerve activity to the mammalian heart and kidney.
879 *Experimental Physiology*, *95*(1), 34-40. https://doi.org/10.1113/expphysiol.2008.046342
880 McMahon, A. P. (2016). Development of the Mammalian Kidney. In (pp. 31-64). Elsevier.
881 https://doi.org/10.1016/bs.ctdb.2015.10.010
882 Meerschaert, K. A., Adelman, P. C., Friedman, R. L., Albers, K. M., Koerber, H. R., & Davis, B. M.
883 (2020). Unique Molecular Characteristics of Visceral Afferents Arising from Different
884 Levels of the Neuraxis: Location of Afferent Somata Predicts Function and Stimulus
885 Detection Modalities. *J Neurosci*, *40*(38), 7216-7228.
886 https://doi.org/10.1523/JNEUROSCI.1426-20.2020
887 Mitchell, G. A. (1950). The nerve supply of the kidneys. *Acta Anat (Basel)*, *10*(1-2), 1-37.
888 https://doi.org/10.1159/000140455
889 Marshall, K. L., et al. (2020). "PIEZO2 in sensory neurons and urothelial cells coordinates
890 urination." Nature 588(7837): 290-295.
891 Mochida, Y., et al. (2022). "Piezo2 expression and its alteration by mechanical forces in mouse
892 mesangial cells and renin-producing cells." Sci Rep 12(1): 4197.
893 Osborn, J. W., & Foss, J. D. (2017). Renal Nerves and Long-Term Control of Arterial Pressure.
894 *Compr Physiol*, *7*(2), 263-320. https://doi.org/10.1002/cphy.c150047
895 Osborn, J. W., Tyshynsky, R., & Vulchanova, L. (2021). Function of Renal Nerves in Kidney
896 Physiology and Pathophysiology. *Annu Rev Physiol*, *83*, 429-450.
897 https://doi.org/10.1146/annurev-physiol-031620-091656
898 Ong, J., et al. (2019). "Renal sensory nerves increase sympathetic nerve activity and blood
899 pressure in 2-kidney 1-clip hypertensive mice." J Neurophysiol 122(1): 358-367.
900 Renier, N., Wu, Z., David, Yang, J., Ariel, P., & Tessier-Lavigne, M. (2014). iDISCO: A Simple,
901 Rapid Method to Immunolabel Large Tissue Samples for Volume Imaging. *Cell*, *159*(4),
902 896-910. https://doi.org/10.1016/j.cell.2014.10.010
903 Sata, Y., Head, G. A., Denton, K., May, C. N., & Schlaich, M. P. (2018). Role of the Sympathetic
904 Nervous System and Its Modulation in Renal Hypertension. *Front Med (Lausanne)*, *5*, 82.
905 https://doi.org/10.3389/fmed.2018.00082
906 Schlaich, M. P., Sobotka, P. A., Krum, H., Lambert, E., & Esler, M. D. (2009). Renal Sympathetic-
907 Nerve Ablation for Uncontrolled Hypertension. *New England Journal of Medicine*,
908 *361*(9), 932-934. https://doi.org/10.1056/nejmc0904179
909 Simon OR, Schramm LP (1983) Spinal Superfusion of Dopamine Excites Renal Sympathetic
910 Nerve Activity. Neuropharmacology 22:287–293.

911 Smith-Anttila, C. J. A., Morrison, V., & Keast, J. R. (2021). Spatiotemporal mapping of sensory
912 and motor innervation of the embryonic and postnatal mouse urinary bladder. *Dev Biol*,
913 *476*, 18-32. https://doi.org/10.1016/j.ydbio.2021.03.008
914 Smyth, I. M. (2021). Monkeying about with Nephron Formation. *J Am Soc Nephrol*, *32*(5), 1011-
915 1013. https://doi.org/10.1681/ASN.2021030320
916 Symplicity, H. T. N. I., Esler, M. D., Krum, H., Sobotka, P. A., Schlaich, M. P., Schmieder, R. E., &
917 Bohm, M. (2010). Renal sympathetic denervation in patients with treatment-resistant
918 hypertension (The Symplicity HTN-2 Trial): a randomised controlled trial. *Lancet*,
919 *376*(9756), 1903-1909. https://doi.org/10.1016/S0140-6736(10)62039-9
920 Stella A, Zanchetti A (1991) Functional Role of Renal Afferents. 71:659–682.
921 Stocker, S. D. and J. B. Sullivan (2023). "Deletion of the Transient Receptor Potential Vanilloid 1
922 Channel Attenuates Sympathoexcitation and Hypertension and Improves Glomerular
923 Filtration Rate in 2-Kidney-1-Clip Rats." Hypertension 80(8): 1671-1682.
924 Tarnick, J., et al. (2023). "Innervation of the developing kidney in vivo and in vitro." Biol Open
925 12(8).
926 Townsend, R. R., Mahfoud, F., Kandzari, D. E., Kario, K., Pocock, S., Weber, M. A., Ewen, S.,
927 Tsioufis, K., Tousoulis, D., Sharp, A. S. P., Watkinson, A. F., Schmieder, R. E., Schmid, A.,
928 Choi, J. W., East, C., Walton, A., Hopper, I., Cohen, D. L., Wilensky, R., . . . investigators*,
929 S. H.-O. M. t. (2017). Catheter-based renal denervation in patients with uncontrolled
930 hypertension in the absence of antihypertensive medications (SPYRAL HTN-OFF MED): a
931 randomised, sham-controlled, proof-of-concept trial. *Lancet*, *390*(10108), 2160-2170.
932 https://doi.org/10.1016/S0140-6736(17)32281-X
933 Tyshynsky, R., et al. (2023). "Periglomerular afferent innervation of the mouse renal cortex."
934 Front Neurosci 17: 974197.
935 Torres, H., et al. (2021). "Sympathetic innervation of the mouse kidney and liver arising from
936 prevertebral ganglia." Am J Physiol Regul Integr Comp Physiol 321(3): R328-R337.
937 Tiniakos, D., et al. (2004). "Ontogeny of intrinsic innervation in the human kidney." Anat
938 Embryol (Berl) 209(1): 41-47.
939 Veelken, R., Vogel, E.-M., Hilgers, K., Amann, K., Hartner, A., Sass, G., Neuhuber, W., & Tiegs, G.
940 (2008). Autonomic Renal Denervation Ameliorates Experimental Glomerulonephritis.
941 *Journal of the American Society of Nephrology*, *19*(7), 1371-1378.
942 https://doi.org/10.1681/asn.2007050552
943 Wickham, H. (2009) Ggplot2: Elegant Graphics for Data Analysis. 2nd Edition, Springer, New
944 York. https://doi.org/10.1007/978-0-387-98141-3
945 Weiss, M. L. and S. I. Chowdhury (1998). "The renal afferent pathways in the rat: a
946 pseudorabies virus study." Brain Res 812(1-2): 227-241.
947 Xiao, L., Kirabo, A., Wu, J., Saleh, M. A., Zhu, L., Wang, F., Takahashi, T., Loperena, R., Foss, J. D.,
948 Mernaugh, R. L., Chen, W., Roberts, J., Osborn, J. W., Itani, H. A., & Harrison, D. G.
949 (2015). Renal Denervation Prevents Immune Cell Activation and Renal Inflammation in
950 Angiotensin II–Induced Hypertension. *Circulation Research*, *117*(6), 547-557.
951 https://doi.org/10.1161/circresaha.115.306010
952 Zheng, M., Chen, R., Chen, H., Zhang, Y., Chen, J., Lin, P., Lan, Q., Yuan, Q., Lai, Y., Jiang, X., Pan,
953 X., & Liu, N. (2018). Netrin-1 Promotes Synaptic Formation and Axonal Regeneration via

JNK1/c-Jun Pathway after the Middle Cerebral Artery Occlusion. *Front Cell Neurosci, 12*, 13. https://doi.org/10.3389/fncel.2018.00013

Figure 1. Kidney innervation commences at E13.5 as axons follow the differentiating arteries and continue to branch throughout development. (A) Pan-neuronal labeling (Tubb3, green) of an E12.5 urogenital system (UGS) shows that renal nerves are absent in the kidney at E12.5 as shown by immunostaining of the branching ureteric bud (cytokeratin, yellow). Ganglion and some postganglionic nerve fibers track along the descending aorta shown by smooth muscle actin (SMA, magenta). **(B)** Pan-neuronal labeling (Tubb3, green) of an E13.5 UGS shows that axons begin to innervate the kidney following the SMA+ vascular mural cells (magenta) of the developing arteries (white arrowhead, zoomed image). CD31 (yellow) highlights the extensive endothelial network that has formed but is yet to be coated with mural cells. **(C)** Axonal projections (Tubb3, green) continue to grow and branch following the developing arterial tree (SMA, magenta) at E16.5. Cytokeratin (yellow) marks the collecting duct system. Multiple axon bundles can be observed on an artery (white arrowhead, zoomed image). **(D)** By E18.5, axons (Tubb3, green) have undergone extensive growth with the arterial tree (SMA, magenta) and additional interstitial branching as the nerves navigate towards and

around kidney structures such as glomeruli (Nphs2, yellow; white arrowhead, zoomed image) A minimum of n=3 kidneys were analyzed for each stage.

Figure 2: Axons associate with kidney structures during embryonic development. (**A)** Image of an E18.5 kidney section immunostained for vasculature (SMA, magenta) and nerves (Tubb3, green). Axons are tightly associated with the SMA+ vasculature. **(B)** Image of an E18.5 kidney section immunostained for nerves (Tubb3, green) and glomeruli (Nphs2, magenta). Axons approach the glomeruli and associate with the Bowman's capsule as they navigate through the kidney. **(C)** Image of an E18.5 kidney section immunostained for nerves (Tubb3, green) and tubule epithelium (Ecad, magenta). Axons are observed closely associating with Ecad^{+} tubules. A minimum of n=3 kidneys were analyzed for each stage.

Figure 3: Nociceptive sensory afferent nerves innervate the developing kidney. (A) Wholemount immunostain of an E16.5 *Trpv1$^{Cre/+}$;R26$^{tdTomato/+}$* kidney showing tdTomato+ (magenta) axons colocalizing with the pan-neuronal marker Tubb3 (green). A magnified inset from the merged shows tdTomato^{+} axons overlapping with Tubb3. **(B)** *Trpv1$^{Cre/+}$;R26$^{tdTomato/+}$* P1 kidney section showing native tdTomato signal (magenta) with immunostained proximal tubules (Lrp2, green) and epithelium (Ecad, yellow). TdTomato+ axons navigate around and closely associate with these structures (white arrowheads). **(C)** *Trpv1$^{Cre/+}$;R26$^{tdTomato/+}$* P1 kidney section showing native tdTomato signal (magenta) with immunostained podocytes (to mark glomeruli, Nphs2, green) and endothelium (CD31, yellow). TdTomato+ axons extend along the vasculature and associate with glomeruli (white arrowhead). A minimum of n=3 kidneys were analyzed for each stage.

Figure 4: Peptidergic and mechanosensory afferent nerves are present in the developing kidney. (A) E15.5 kidney section immunostained for the neuropeptide CGRP^{+} (magenta) and pan-neuronal marker Tubb3 (green). CGRP^{+} nerves mainly associate with the kidney vasculature (CD31, yellow; white arrowhead) at this stage. **(B)** Sections of *Pod-Cre$^{tg/+}$;R26$^{tdTomato/tdTomato}$* P0 kidneys immunostained for CGRP^{+}

(magenta). CGRP+ axons are found near (white arrowhead) glomeruli (tdTomato, green) and close to proximal tubules (Lrp2, yellow). **(C)** Adult kidney section immunostained for CGRP (magenta) and colocalized with Tubb3 (green) shows $CGRP^+$ axons closely associating with the vasculature (CD31, yellow) and in close proximity to glomeruli (white arrowhead). **(D)** E18.5 kidney section immunostained for substance P (SubP, magenta) shows overlap with Tubb3 (green). $SubP^+$ nerves were found associated with the vasculature (CD31, yellow, white arrowhead). **(E)** Adult kidney section immunostained for $SubP^+$ (magenta) and Tubb3 (green) shows SubP+ nerves along the vasculature (CD31, yellow) and in close proximity to glomeruli (white arrowhead). **(F)** E15.5 kidney section immunostained for Piezo2 (magenta) and Tubb3 (green) show Piezo2+ nerves associating with the vasculature (CD31, yellow; white arrowhead). **(G)** Sections of *Pod-Cre*$^{tg/+}$*;R26*$^{tdTomato/tdTomato}$ P0 kidneys immunostained for Piezo2 (magenta) show Piezo2+ nerves closely associating (white arrowheads) with glomeruli (tdTomato, green) and proximal tubules (Lrp2, yellow). A minimum of n=3 kidneys were analyzed for each stage.

Figure 5: CTB retrograde tracing shows axon trajectories and labeling of thoracic, lumbar, and sacral DRGs. (A) Schematic of retrograde tracing injection and timeline. CTB-555 was injected into the right kidney of adult mice. Three days following the injection both kidneys were dissected as well as the ipsilateral DRGs (injected side) and contralateral DRGs (non-injected side). **(B)** Sensory innervation primarily traces in the ipsilateral DRGs to the lower thoracic region (T10-T13), lumbar region (L1-L6), and sacral region (S1-S2). Tracing to the contralateral DRGs was observed in the upper lumbar region of L1 and L2. n=4 males and n=4 females, Scale bar =50µm. **(C)** Ipsilateral and contralateral kidney sections of CTB-injected kidneys. Immunostaining of the ipsilateral kidney section showed CTB^+ staining (magenta) colocalizing with Tubb3 (green) near glomeruli (CD31, yellow, arrowhead) and vasculature (CD31, yellow). CTB^+ staining (magenta, arrowhead) colocalized with Tubb3 (green) near vasculature (CD31, yellow) in the contralateral (non-injected) kidney. **(D)** Schematic representation of the spinal level and DRG origin of kidney sensory afferent innervation.

Figure 6: Noradrenergic sympathetic nerves innervate the developing kidney. (A) E14.5 wholemount immunostained kidney labeled with tyrosine hydroxylase (TH, magenta) shows that the first innervating axons (Tubb3, green) are TH+. Cytokeratin (yellow) marks the developing collecting duct system. **(B)** P0 wholemount immunostained kidney labeled with TH (magenta) shows that the TH+ nerves have branched extensively alongside the arterial tree (SMA, green). Lrp2 marks the proximal tubules (yellow) and the magnified inset shows TH^+ nerves (magenta) navigating around and in close proximity to proximal tubules (white arrowheads). **(C)** E15.5 kidney section immunostained for TH (magenta) and Tubb3 (green) shows TH+ axons around the vasculature (CD31, yellow; white arrowhead). **(D)** Sections of *Pod-Cre*$^{tg/+}$*;R26*$^{tdTomato/tdTomato}$ P0 kidneys immunostained for TH (magenta) show TH^+ axons near glomeruli (tdTomato, green; white arrowhead) and proximal tubules (Lrp2, yellow)**.** A minimum of n=3 kidneys were analyzed for each stage.

Figure 7: Nerves form putative neuroeffector-junctions with kidney targets during development. (A) Immunostaining of E14.5 kidney sections for synapsin I (Syn1, magenta) shows overlap with Tubb3 (green) and association of axons with the main artery (CD31, yellow; white arrowhead). **(B)** E15.5 kidney sections immunostained for Syn1 (magenta) and Tubb3 (green) similarly show $Syn1^+$ nerves positive around the vasculature (CD31, yellow). **(C)** Sections of *Pod-Cre*$^{tg/+}$*;R26*$^{tdTomato/tdTomato}$ P0 kidneys immunostained for Syn1 (magenta) show Syn1+ axons (Tubb3, green) near glomeruli (tdTomato, green; white arrowheads, top panel) and proximal tubules (Lrp2, yellow; White arrowhead, bottom panel). **(D)** Sections of *Pod-Cre*$^{tg/+}$*;R26*$^{tdTomato/tdTomato}$ adult kidneys immunostained for Syn1 (magenta) show Syn1+ axons (Tubb3, green) along the arterioles near glomeruli (tdTomato, green; white arrowhead). A minimum of n=3 kidneys were analyzed for each stage.

Figure 8: Sympathetic and sensory nerves show similar structural associations in the adult human kidney. (A) Adult human kidney sections immunostained for TH^+ sympathetic nerves (green) can be observed associating with glomeruli shown by Podocalyxin (magenta; top panel, white arrowhead) and in close proximity to epithelial

structures (ECAD, yellow; bottom panel, white arrowhead). **(B)** Adult human kidney sections immunostained for PIEZO2 (magenta) show PIEZO2^{+} overlapping with TUBB3 (green) associating with glomeruli (Podocalyxin, yellow; white arrowhead, top panel) and the vasculature (Podocalyxin, yellow; white arrowhead, middle panel). PIEZO2+ sensory nerves were also observed near epithelial structures (LRP, green; ECAD, yellow; white arrowhead, bottom panel). **(C)** Adult human kidney sections immunostained for SYN1 (green) show SYN1+ axons near glomeruli (Podocalyxin, magenta; white arrowhead, top panel) and epithelial structures (ECAD, yellow; white arrowhead, bottom panel).

Figure S1: Innervation of the embryonic and postnatal kidney. (A) Wholemount immunostain of an E14.5 kidney for Tubb3 (green), SMA (red), and CD31 (grey). Axons track closely with the developing arteries despite the presence of an extensive CD31+ endothelial network. (**B)** Wholemount immunostain of a P0 kidney for Tubb3 (green), Nphs2 (podocytes, magenta), and Lrp2 (proximal tubules, yellow). The neuronal network continues to expand and navigate towards and around kidney structures. **(C)** Wholemount immunostain of a P0 kidney for Tubb3 (green), SMA (red), and Nphs2 (podocytes, grey). The neuronal network has continued to grow as the vasculature expands and the last wave of nephrons differentiate.

Figure S2: Delay in renal peptidergic sensory innervation and innervation timeline of mechanosensitive axons in the metanephric kidney. (A) E14.5 kidney sections immunostained for CGRP (magenta) shows that axons at this stage (Tubb3, green) that primarily associate with the vasculature (CD31, yellow) are not yet CGRP+. **(B)** E14.5 kidney sections immunostained for substance P (SubP, magenta) shows that axons at this stage (Tubb3, green) that primarily associate with the vasculature (CD31, yellow) are not yet SubP+.

Figure S3: pAAV-Flex retrograde tracing of Piezo2^{+} sensory nerves show labeling of lower thoracic and upper lumbar DRGs. (A) Schematic of retrograde tracing injections and timeline. pAAV-Flex-tdTomato was injected into the right kidney of

Piezo2$^{GFPCre/+}$ mice. Three weeks following ipsilateral (injected side) and contralateral (non-injected side) DRGs were collected for analysis. **(B)** Piezo2^{+} renal sensory innervation primarily traces in the ipsilateral DRG in the lower thoracic region (T10-T13) and the upper lumbar region (L1-L2). Scale = 50µm. **(C)** Schematic representation of the spinal level and DRG origin of kidney Piezo2+ sensory afferent innervation

Figure S4: The cholinergic marker VAChT labels axons in the developing kidney. (A) E14.5 kidney sections immunostained for VAChT (magenta), Tubb3 (green), and CD31 (endothelium) show that axons (white arrowhead) are not positive for VAChT at this stage. VAChT signal is primarily background, non-specific signal. **(B)** E15.5 kidney sections immunostained for VAChT (magenta), Tubb3 (green), and CD31 (endothelium) show that VAChT signal (white arrowhead) is similar to Tubb3 axonal signal (green). **(C)** Sections of *Pod-Cre*$^{tg/+}$*;R26*$^{tdTomato/tdTomato}$ P0 kidneys immunostained for VAChT (magenta) show VAChT+ axons near glomeruli (tdTomato, green; white arrowheads, top panel) and proximal tubules (Lrp2, yellow; White arrowhead, bottom panel). **(D)** Adult kidney sections immunostained for VAChT (magenta), Tubb3 (green), and CD31 (endothelium) show that VAChT signal overlaps with Tubb3 and closely associates with the vasculature.

Figure S5: Differential enrichment of adrenergic, purinergic, and post-synaptic markers within the different cell clusters of the E18.5 kidney (A) Heatmaps showing relative enrichment of adrenergic receptors in the different kidney cell types (clusters) from E18.5 whole kidney scRNA-seq data (Combes et al., 2019). **(B)** Heatmaps showing relative enrichment of purinergic receptors in the different kidney cell types (clusters) at E18.5. **(C)** Heatmaps showing relative enrichment of post-synaptic markers in the different kidney cell types (clusters) at E18.5. The scale indicates log fold change relative to the other cell clusters. NP=nephron progenitor, NP (STR) = nephron progenitor and stroma related, PTA = pretubular aggregate, RV = renal vesicle, SSB = S-shaped body, DT = distal tubule, EPT = early proximal tubule, PT = proximal tubule, Pod = podocytes, UE = ureteric epithelium, Str-CS = cortical stroma, Str-MS =

medullary stroma, Str-CD = collecting duct stroma, Str-Ur = ureteric stroma, Imm = immune cells, Endo = endothelium. LogFC DE = log fold change differential expression.

Suppl. Table 1: Wholemount tissue processing steps for iDISCO^{+} and light-sheet microscopy

Suppl. Table 2: Imaging parameters utilized in this study

Suppl. Table 3: List of primary antibodies used in this study

Figure 1

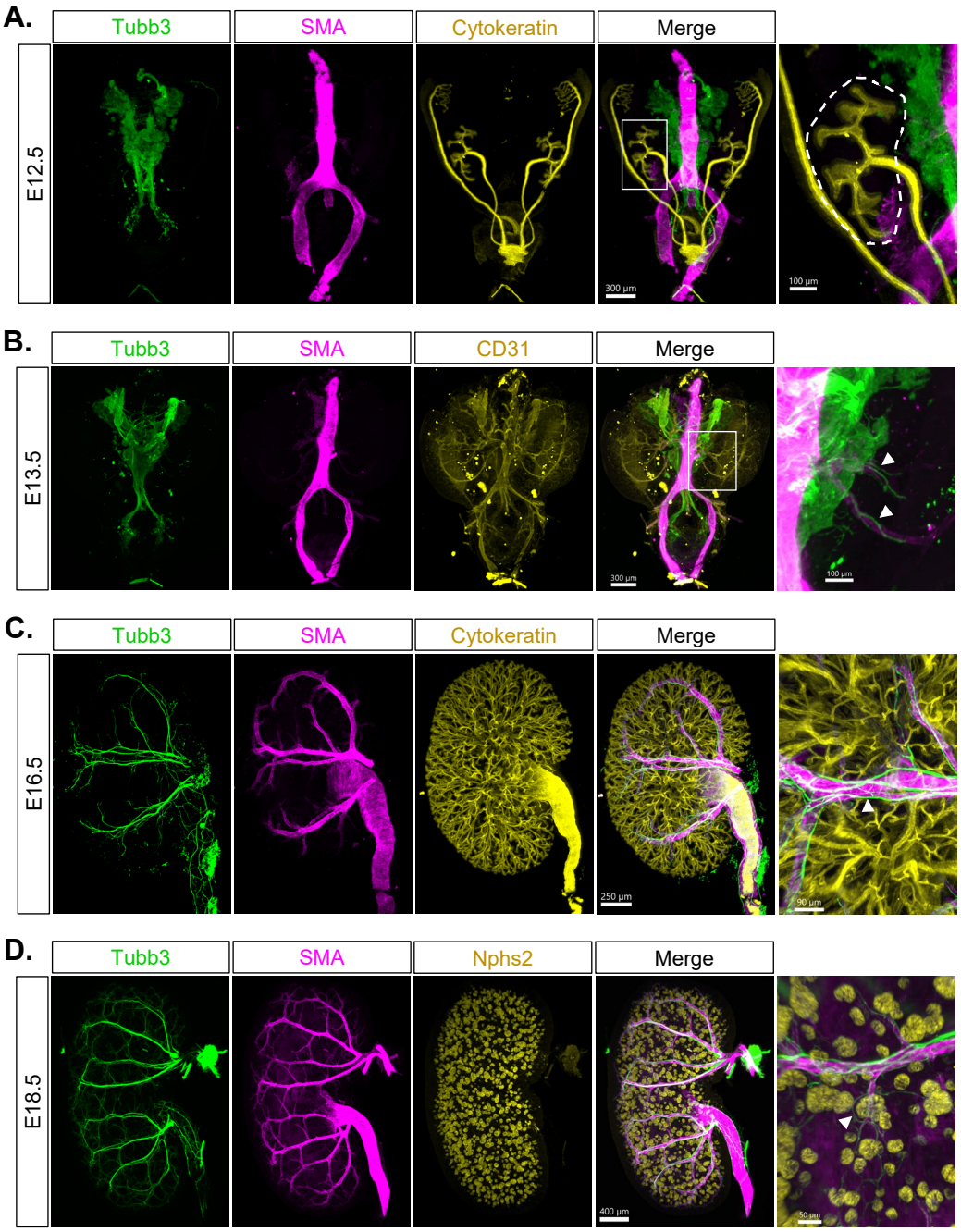
A.
Tubb3
SMA
Cytokeratin
Merge
E12.5
300 µm
100 µm
B.
Tubb3
SMA
CD31
Merge
E13.5
300 µm
100 µm
C.
Tubb3
SMA
Cytokeratin
Merge
E16.5
250 µm
90 µm
D.
Tubb3
SMA
Nphs2
Merge
E18.5
400 µm
50 µm

Figure 2

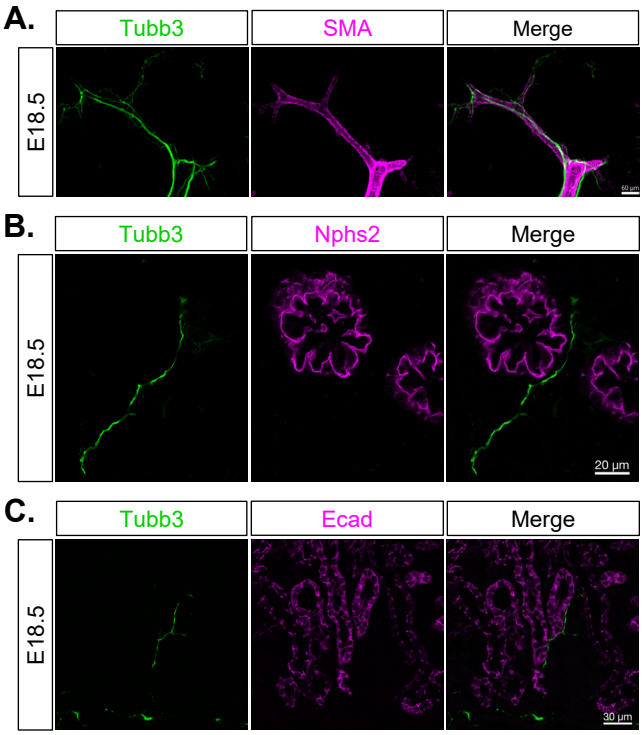
A.
Tubb3
SMA
Merge
E18.5
B.
Tubb3
Nphs2
Merge
E18.5
20 µm
C.
Tubb3
Ecad
Merge
E18.5
30 µm

Figure 3

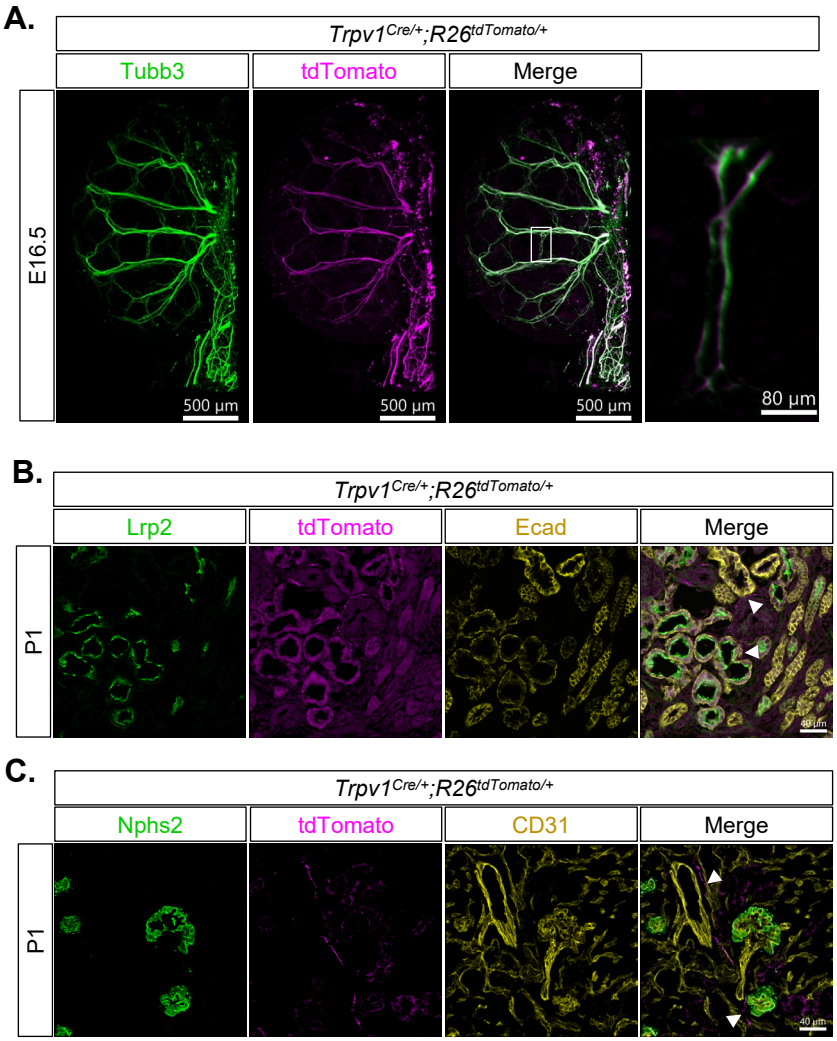
A.
Trpv1Cre/+;R26tdTomato/+
Tubb3
tdTomato
Merge
E16.5
500 µm
500 µm
500 µm
80 µm
B.
Trpv1Cre/+;R26tdTomato/+
Lrp2
tdTomato
Ecad
Merge
P1
40 µm
C.
Trpv1Cre/+;R26tdTomato/+
Nphs2
tdTomato
CD31
Merge
P1
40 µm

Figure 4

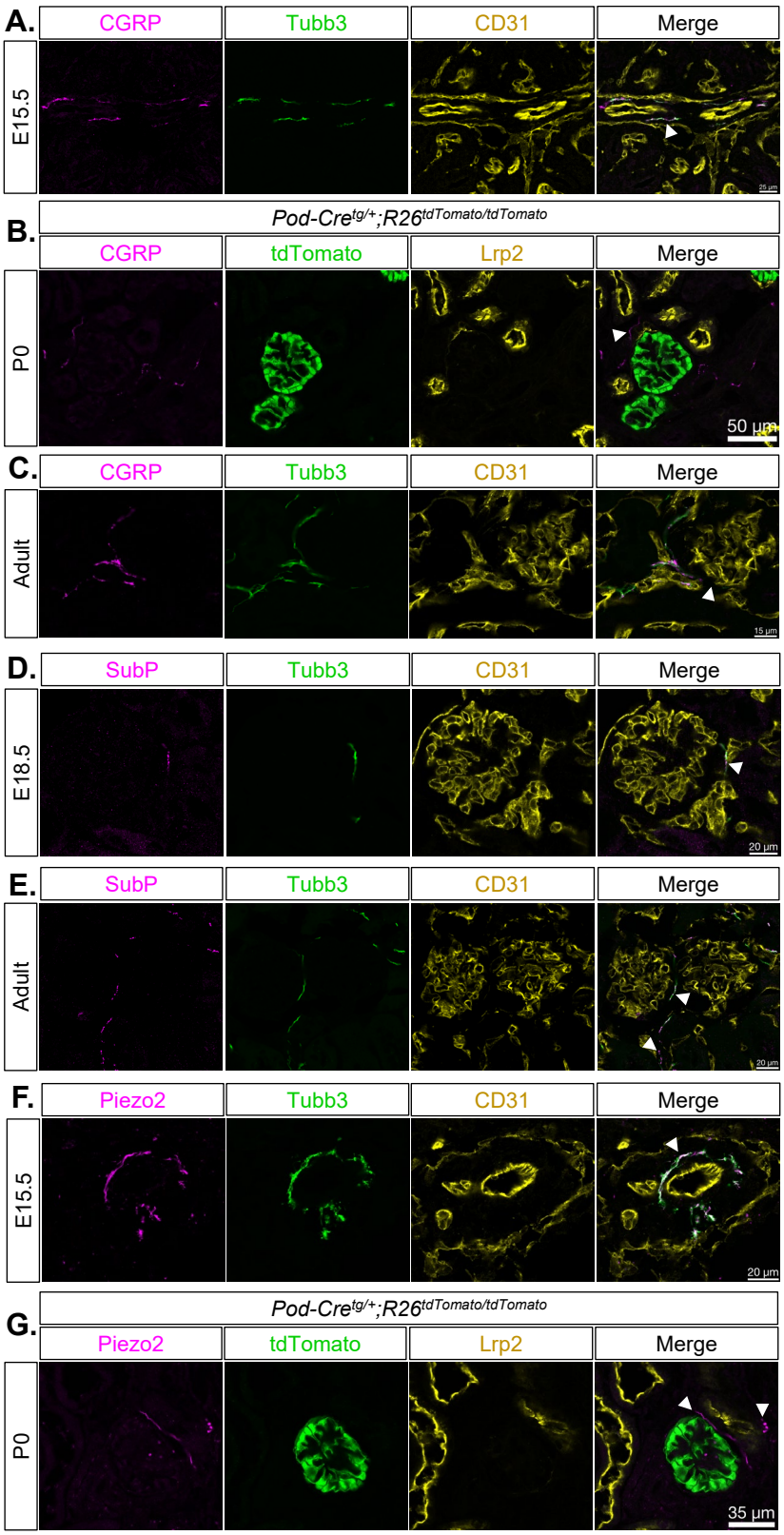
A.
CGRP
Tubb3
CD31
Merge
E15.5
25 µm
B.
Pod-Cre tg/+;R26 tdTomato/tdTomato
CGRP
tdTomato
Lrp2
Merge
P0
50 µm
C.
CGRP
Tubb3
CD31
Merge
Adult
15 µm
D.
SubP
Tubb3
CD31
Merge
E18.5
20 µm
E.
SubP
Tubb3
CD31
Merge
Adult
20 µm
F.
Piezo2
Tubb3
CD31
Merge
E15.5
20 µm
G.
Pod-Cre tg/+;R26 tdTomato/tdTomato
Piezo2
tdTomato
Lrp2
Merge
P0
35 µm

Figure 5

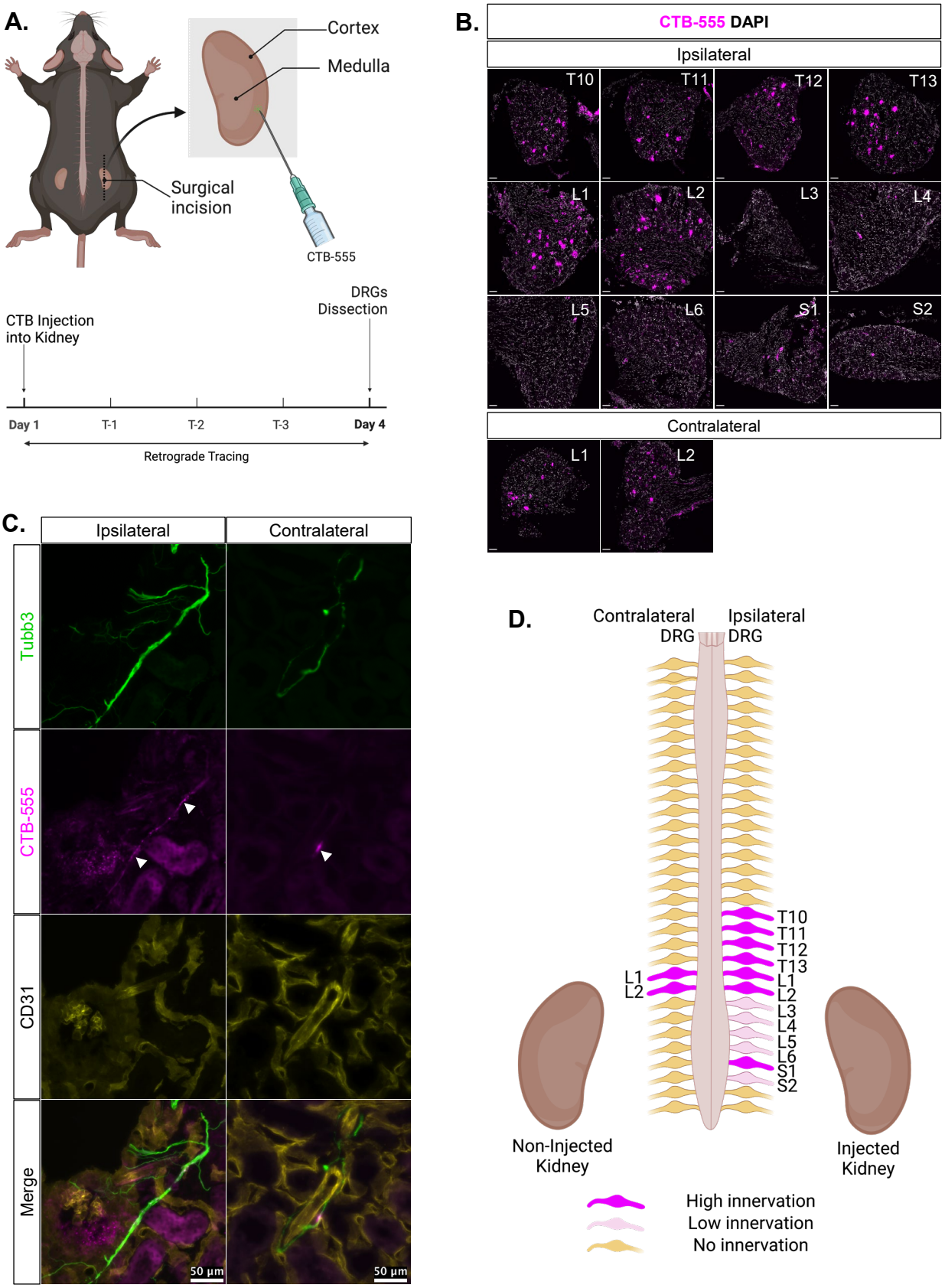
A.
Cortex
Medulla
Surgical incision
CTB-555
DRGs Dissection
CTB Injection into Kidney
Day 1
T-1
T-2
T-3
Day 4
Retrograde Tracing
B.
CTB-555 DAPI
Ipsilateral
T10
T11
T12
T13
L1
L2
L3
L4
L5
L6
S1
S2
Contralateral
L1
L2
C.
Ipsilateral
Contralateral
Tubb3
CTB-555
CD31
Merge
50 µm
50 µm
D.
Contralateral DRG
Ipsilateral DRG
T10
T11
T12
T13
L1
L2
L1
L2
L3
L4
L5
L6
S1
S2
Non-Injected Kidney
Injected Kidney
High innervation
Low innervation
No innervation

Figure 6

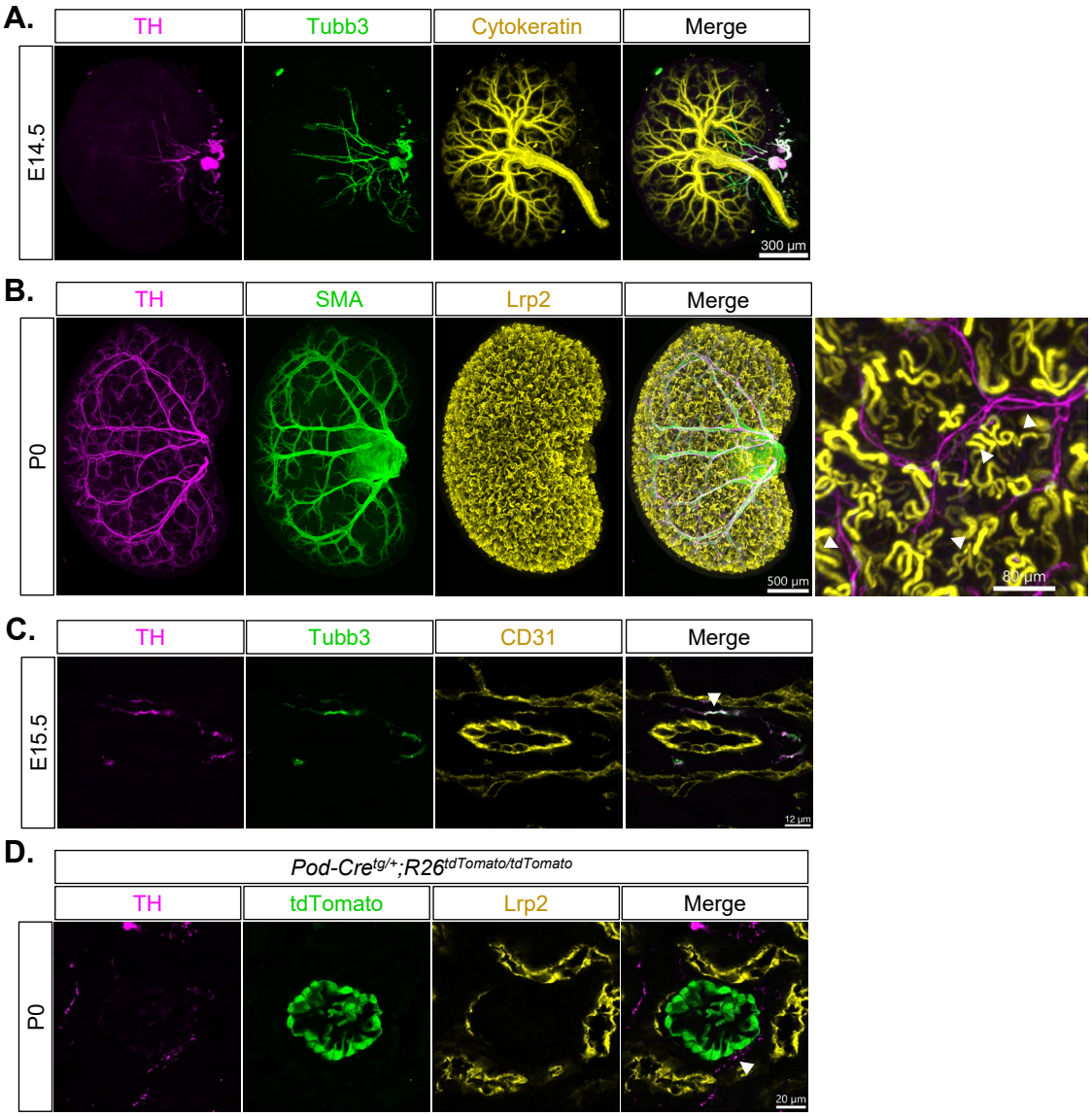
A.
TH
Tubb3
Cytokeratin
Merge
E14.5
300 µm
B.
TH
SMA
Lrp2
Merge
P0
500 µm
80 µm
C.
TH
Tubb3
CD31
Merge
E15.5
12 µm
D.
Pod-Cretg/+;R26tdTomato/tdTomato
TH
tdTomato
Lrp2
Merge
P0
20 µm

Figure 7

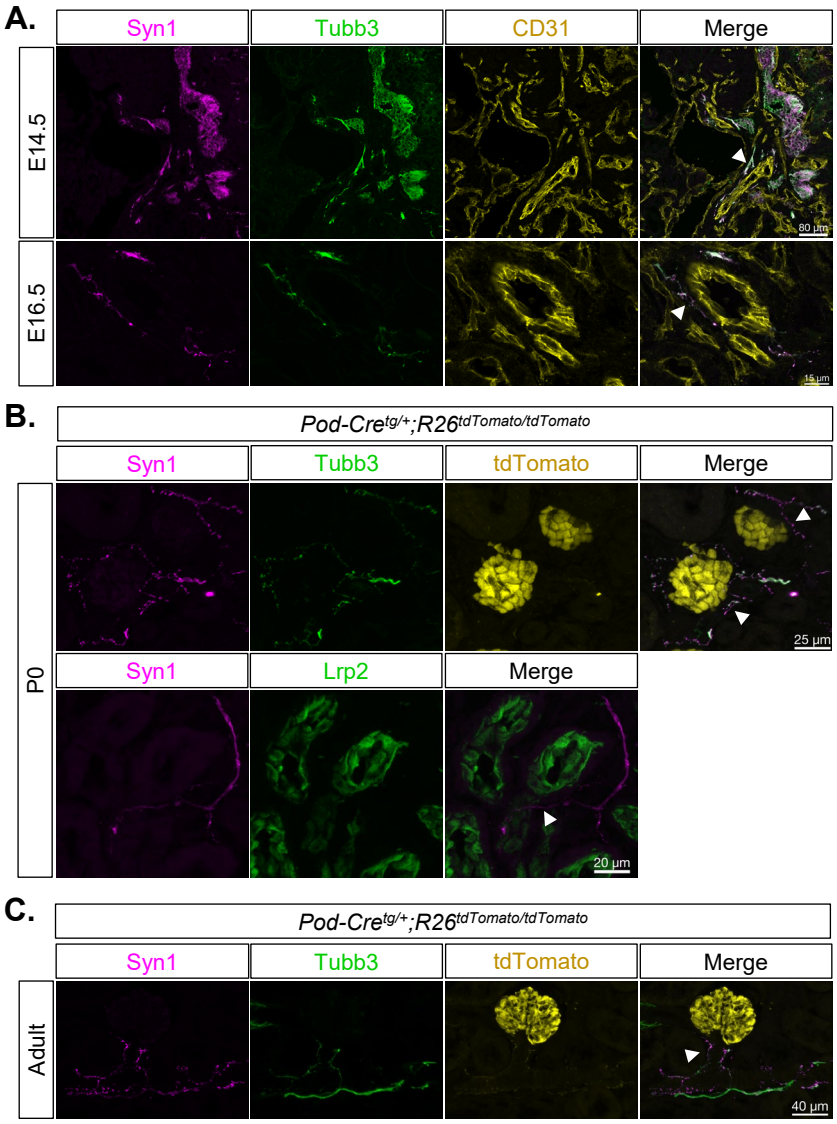
A.
Syn1
Tubb3
CD31
Merge
E14.5
E16.5
80 µm
15 µm
B.
Pod-Cretg/+;R26tdTomato/tdTomato
Syn1
Tubb3
tdTomato
Merge
P0
25 µm
Syn1
Lrp2
Merge
20 µm
C.
Pod-Cretg/+;R26tdTomato/tdTomato
Syn1
Tubb3
tdTomato
Merge
Adult
40 µm

Figure 8

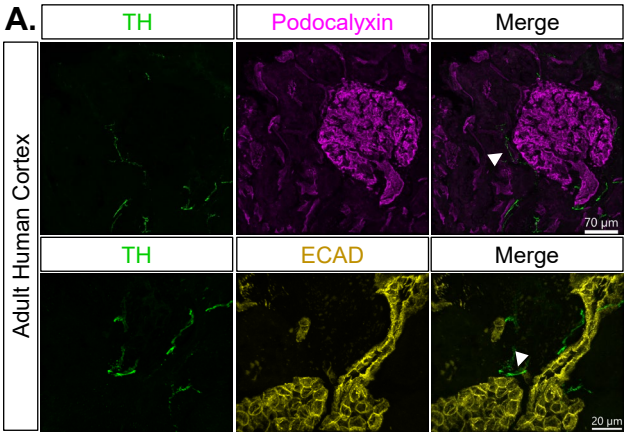
A.
TH
Podocalyxin
Merge
Adult Human Cortex
70 µm
TH
ECAD
Merge
20 µm

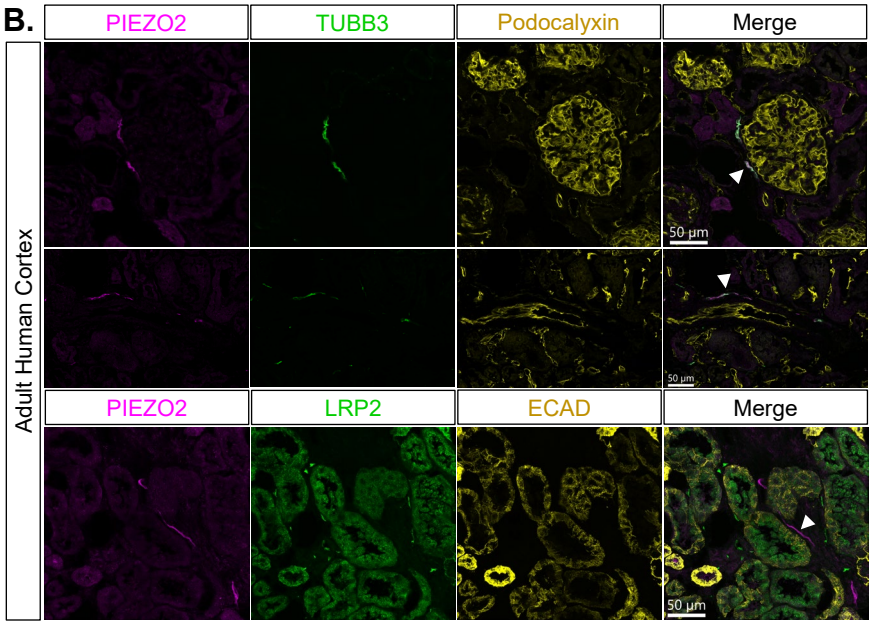
B.
PIEZO2
TUBB3
Podocalyxin
Merge
Adult Human Cortex
50 µm
PIEZO2
LRP2
ECAD
Merge
50 µm

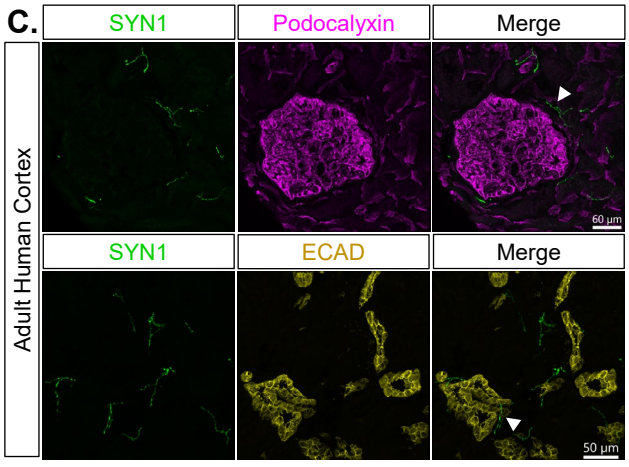
C.
SYN1
Podocalyxin
Merge
Adult Human Cortex
60 µm
SYN1
ECAD
Merge
50 µm

Figure S1

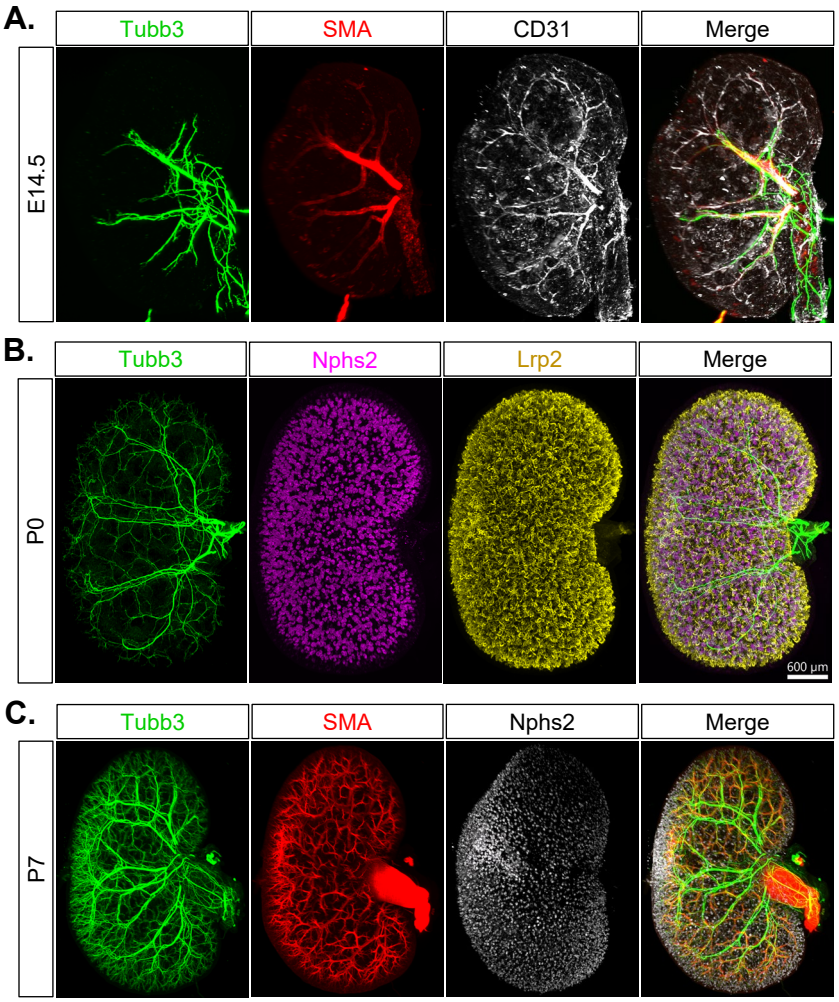
A.
Tubb3
SMA
CD31
Merge
E14.5
B.
Tubb3
Nphs2
Lrp2
Merge
P0
600 µm
C.
Tubb3
SMA
Nphs2
Merge
P7

Figure S2

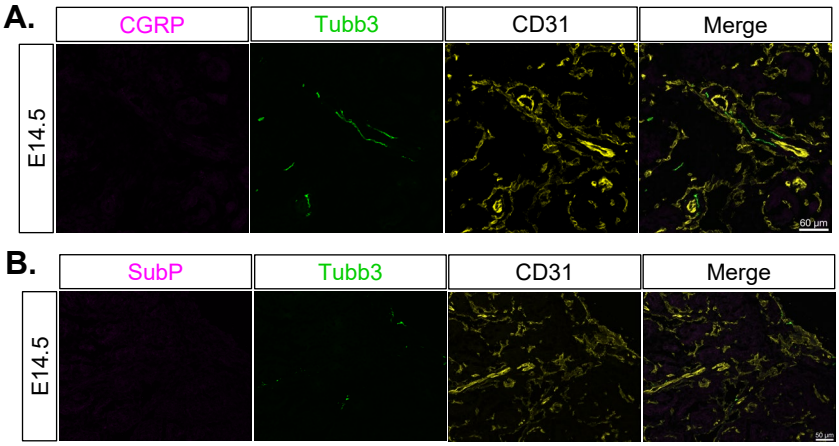
A.
CGRP
Tubb3
CD31
Merge
E14.5
60 µm
B.
SubP
Tubb3
CD31
Merge
E14.5
50 µm

Figure S3

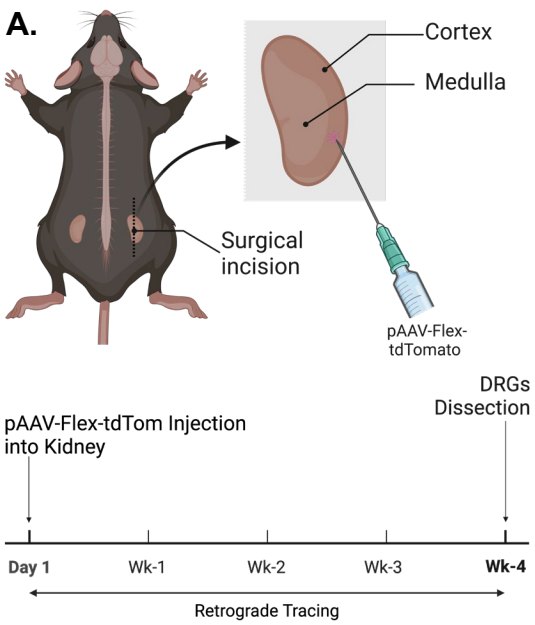
A.
Cortex
Medulla
Surgical incision
pAAV-Flex-tdTomato
DRGs Dissection
pAAV-Flex-tdTom Injection into Kidney
Day 1
Wk-1
Wk-2
Wk-3
Wk-4
Retrograde Tracing

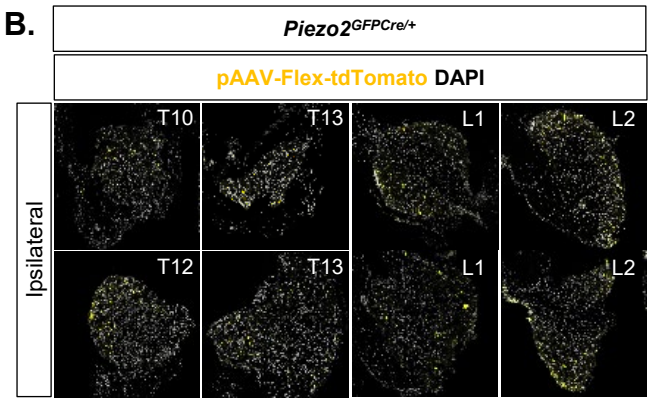
B.
Piezo2GFPCre/+
pAAV-Flex-tdTomato DAPI
Ipsilateral
T10
T13
L1
L2
T12
T13
L1
L2

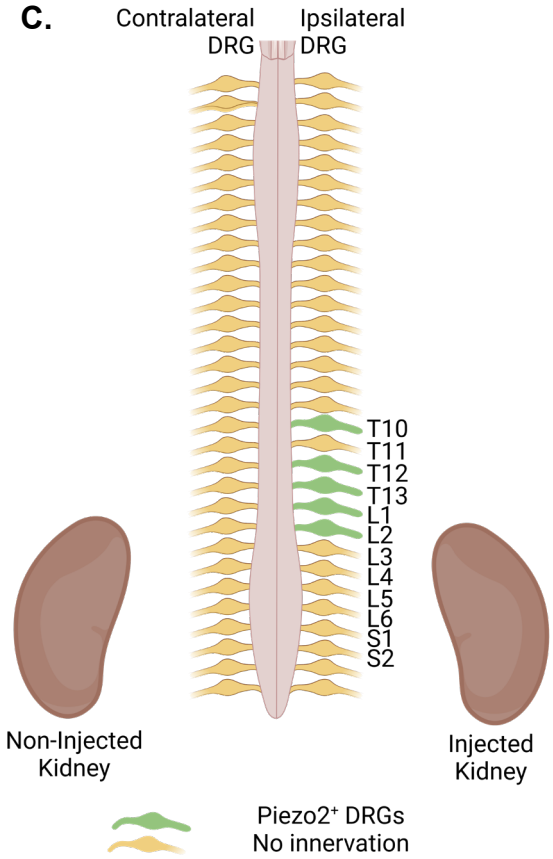
C.
Contralateral DRG
Ipsilateral DRG
T10
T11
T12
T13
L1
L2
L3
L4
L5
L6
S1
S2
Non-Injected Kidney
Injected Kidney
Piezo2+ DRGs
No innervation

Figure S4

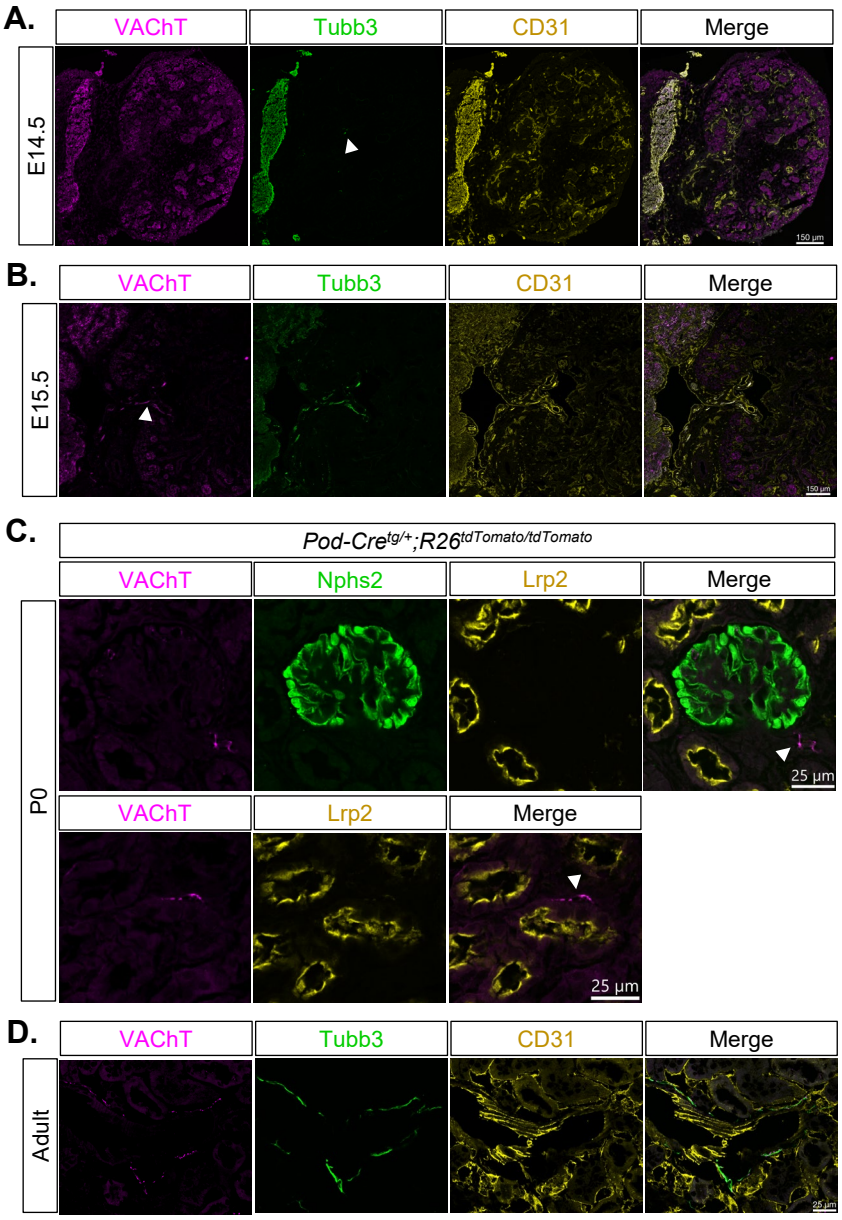
A.
VAChT
Tubb3
CD31
Merge
E14.5
150 µm
B.
VAChT
Tubb3
CD31
Merge
E15.5
150 µm
C.
Pod-Cre tg/+;R26 tdTomato/tdTomato
VAChT
Nphs2
Lrp2
Merge
P0
25 µm
VAChT
Lrp2
Merge
25 µm
D.
VAChT
Tubb3
CD31
Merge
Adult
25 µm

Figure S5

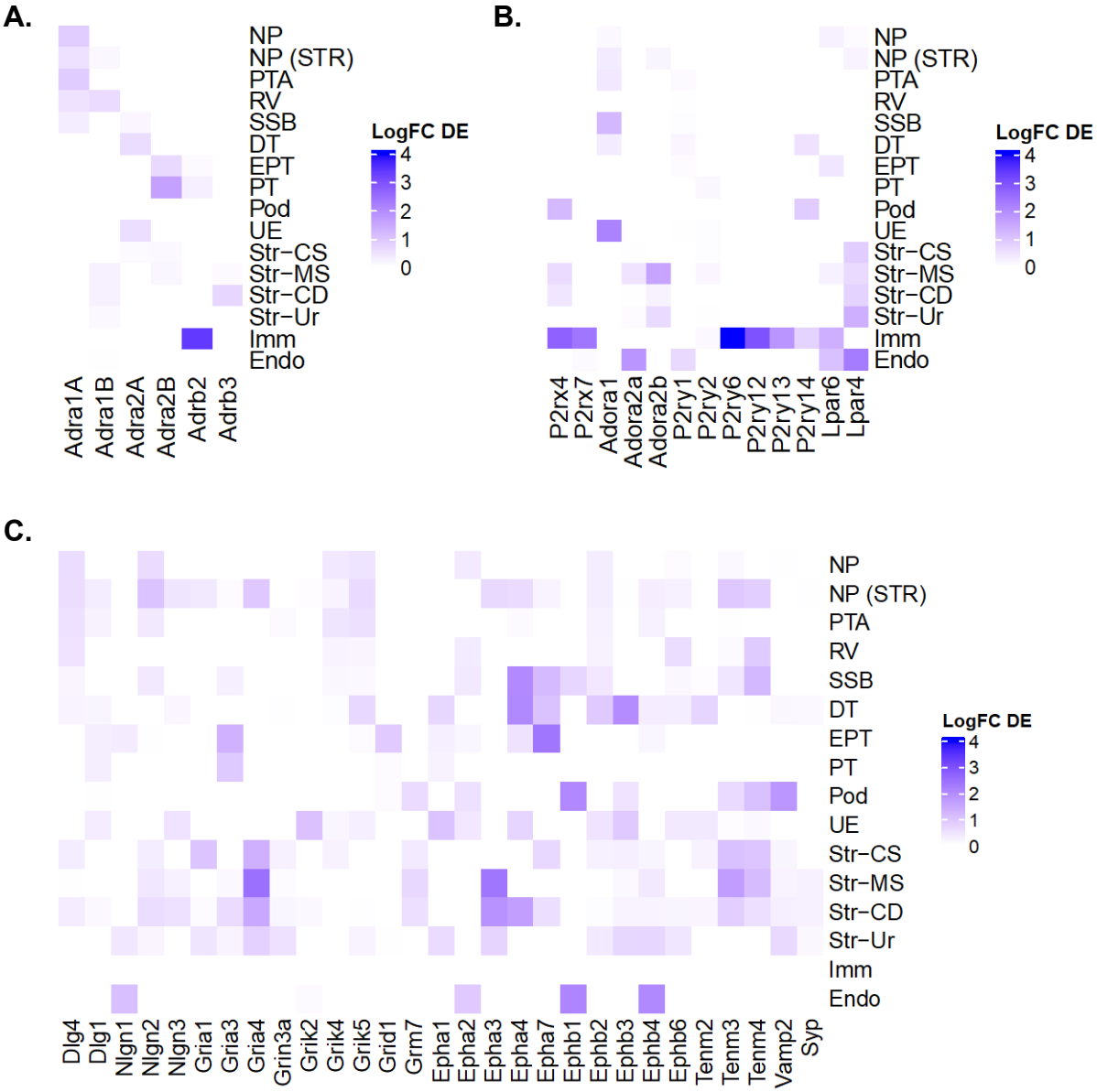
A.
NP
NP (STR)
PTA
RV
SSB
DT
EPT
PT
Pod
UE
Str−CS
Str−MS
Str−CD
Str−Ur
Imm
Endo
Adra1A
Adra1B
Adra2A
Adra2B
Adrb2
Adrb3
LogFC DE
4
3
2
1
0
B.
P2rx4
P2rx7
Adora1
Adora2a
Adora2b
P2ry1
P2ry2
P2ry6
P2ry12
P2ry13
P2ry14
Lpar6
Lpar4
C.
Dlg4
Dlg1
Nlgn1
Nlgn2
Nlgn3
Gria1
Gria3
Gria4
Grin3a
Grik2
Grik4
Grik5
Grid1
Grm7
Epha1
Epha2
Epha3
Epha4
Epha7
Ephb1
Ephb2
Ephb3
Ephb4
Ephb6
Tenm2
Tenm3
Tenm4
Vamp2
Syp

Supplementary Table 1

Steps		Modality	Time	Temperature	Volume (mL)
1	Blocking: PBS, 10% (v/v) HISS, 0.5% (v/v) Triton-x 100	passive perfusion on rocker cover from light	1hr	RT	1mL/Kidney pair
2	Primary Antibody Solution: PBS, 10% (v/v) HISS, 0.5% (v/v) Triton-x 100, Primary antibody	passive perfusion on rocker cover from light	7 days	4℃	1mL/Kidney pair
3	Wash Solution: PBS, 0.25% (v/v) Triton-x 100	passive perfusion on rocker cover from light	1 days	RT	1mL/Kidney pair
4	Secondary Antibody Solution: PBS, 10% (v/v) HISS, 0.5% (v/v) Triton-x 100, Secondary antibody	passive perfusion on rocker cover from light	3.5 days	4℃	1mL/Kidney pair
5	Wash Solution: PBS, 0.25% (v/v) Triton-x 100	passive perfusion on rocker cover from light	1 days	RT	1mL/Kidney pair
6	Embed kidneys in 1% Agarose gel to a 5x5mm block	n/a			
7	Methanol Dehydration: 25% (v/v) Methanol in water	passive perfusion on rocker cover from light	1hr	RT	5mL/Kidney pair
8	Methanol Dehydration: 50% (v/v) Methanol in water	passive perfusion on rocker cover from light	1hr	RT	5mL/Kidney pair
9	Methanol Dehydration: 75% (v/v) Methanol in water	passive perfusion on rocker cover from light	1hr	RT	5mL/Kidney pair
10	Methanol Dehydration: 100% (v/v) Methanol	passive perfusion on rocker cover from light	1hr	RT	5mL/Kidney pair
11	DCM Dehydration: 66% (v/v) DCM/33% (v/v) Methanol	passive perfusion on rocker cover from light	3hrs	RT	5mL/Kidney pair
12	DCM Dehydration: 100% (v/v) DCM	passive perfusion on rocker cover from light	15min	RT	5mL/Kidney pair
13	DCM Dehydration: 100% (v/v) DCM	passive perfusion on rocker cover from light	15min	RT	5mL/Kidney pair
14	100% (v/v) DBE Incubation	cover from light	Indefinitly	RT	5mL/Kidney pair

Supplementary Table 2

Figures		System	Objective Specifications						Acquisition/Visualisation Prameters			Data size
			Magnification	NA	RI	WD	Zoom	Total Magnifdication	Image pixel size	Z-step	Note	
Figures												
1	A	UM II	2x; corr.-3.5	0.016	1.56	5.7mm	3.2x	6.4	0.95 µm/pixel	1.4µm	3D recontruction; Maximum intensity projection	47.8 GB
	B	UM II	2x; corr.-3.5	0.016	1.56	5.7mm	2.5x	5.0	1.22 µm/pixel	1.4µm	3D recontruction; Maximum intensity projection	38.8 GB
	C	UM II	2x; corr.-3.5	0.016	1.56	5.7mm	4x	8.0	0.75 µm/pixel	1.4µm	3D recontruction; Maximum intensity projection	40.0 GB
	D	UM II	2x; corr.-3.5	0.016	1.56	5.7mm	2.5x	5.0	1.22 µm/pixel	1.4µm	3D recontruction; Maximum intensity projection	59.8 GB
2	A	A.D. SDC	25x	0.95	1.33	2.4mm	n.a	25x			3D recontruction; Maximum intensity projection	4.82 GB
	B	LSM 880	40x oil	1.3	1.51	0.21mm	n.a	40	0.08 µm/pixel	n.a	2D single slice	26.29 MB
	C	LSM 880	40x oil	1.3	1.51	0.21mm	n.a	40	0.42 µm/pixel	n.a	Tile Scan 2x2; 2D single slice	8.2 MB
3	A	UM II	2x; corr.-3.5	0.016	1.56	5.7mm	4x	8.0	0.75 µm/pixel	1.4µm	3D recontruction; Maximum intensity projection	55.9 GB
	B	LSM 880	20x	0.8	1.0	0.55mm	n.a	20	0.12 µm/pixel	n.a	2D single slice	40.28 MB
	C	LSM 880	20x	0.8	1.0	0.55mm	n.a	20	0.12 µm/pixel	7.9µm	3D recontruction; Maximum intensity projection	360.88 MB
4	A	LSM 880	20x	0.8	1.0	0.55mm	n.a	20	0.12 µm/pixel	n.a	Tile Scan 2x2; 2D single slice	160.53 MB
	B	LSM 900	40x oil	1.4	1.51	0.13mm	n.a	40	0.07 µm/pixel	n.a	Tile Scan 3x3; 2D single slice	454.14 MB
	C	LSM 880	40x oil	1.3	1.51	0.21mm	n.a	40	0.08 µm/pixel	n.a	2D single slice	59.81 MB
	D	LSM 880	40x oil	1.3	1.51	0.21mm	n.a	40	0.08 µm/pixel	n.a	2D single slice	26.68 MB
	E	LSM 880	40x oil	1.3	1.51	0.21mm	n.a	40	0.08 µm/pixel	n.a	Tile Scan 2x2; 2D single slice	106.24 MB
	F	LSM 880	40x oil	1.3	1.51	0.21mm	n.a	40	0.08 µm/pixel	n.a	Tile Scan 2x2; 2D single slice	106.23 MB
	G	LSM 900	40x oil	1.4	1.51	0.13mm	n.a	40	0.07 µm/pixel	n.a	2D single slice	40.17 MB
5	B	LSM 780	20x	0.8	1.0	0.55mm	0.6	20x	0.69 µm/pixel	n.a	2D single slice	4226 KB
	C	DMi8	20x DMi8	0.4	1.0	6.2-7.5 mm	n.a	20x	0.32 µm/pixel	n.a	2D single slice, Ipsilateral kidney image	38.1 MB
		DMi8	20x DMi8	0.4	1.0	6.2-7.5 mm	n.a	20x	0.32 µm/pixel	n.a	2D single slice, Cintralateral kidney image	36.6 MB
6	A											
	B	UM II	2x; corr.-3.5	0.016	1.56	5.7mm	2x	4	1.54 µm/pixel	2.0µm	3D recontruction; Maximum intensity projection	49.2 GB
	C	LSM 880	40x oil	1.3	1.51	0.21mm	n.a	40	0.08 µm/pixel	n.a	2D single slice	26.68 MB
	D	LSM 900	40x oil	1.4	1.51	0.13mm	n.a	40	0.07 µm/pixel	n.a	2D single slice	40.17 MB
	E	LSM 900	40x oil	1.4	1.51	0.13mm	n.a	40	0.07 µm/pixel	n.a	Tile Scan 2x2; 2D single slice	203.39 MB
7	A	LSM 880	20x	0.8	1.0	0.55mm	n.a	20	0.12 µm/pixel	n.a	2D single slice	144.91 MB
		LSM 880	40x oil	1.3	1.51	0.21mm	n.a	40	0.08 µm/pixel	n.a	2D single slice	26.68 MB
	B	LSM 880	20x	0.8	1.0	0.55mm	n.a	20	0.12 µm/pixel	0.90µm	3D recontruction; Maximum intensity projection	361.31 MB
		LSM 880	40x oil	1.3	1.51	0.21mm	n.a	40	0.08 µm/pixel	0.50µm	Tile Scan 2x2; 3D recontruction; Maximum intensity projection	3.11 GB
	C	LSM 880	20x	0.8	1.0	0.55mm	n.a	20	0.12 µm/pixel	0.90µm	3D recontruction; Maximum intensity projection	920.56 MB
8	A	LSM 880	40x oil	1.3	1.51	0.21mm	n.a	40	0.08 µm/pixel	1.8µm	Tile Scan 3x3; 3D recontruction; Maximum intensity projection	3.96 GB
	B	LSM 880	40x oil	1.3	1.51	0.21mm	n.a	40	0.08 µm/pixel	n.a	Tile Scan 2x2; 2D Single slice	106.23 MB
		LSM 880	40x oil	1.3	1.51	0.21mm	n.a	40	0.08 µm/pixel	n.a	Tile Scan 3x2; 2D Single slice	159.22 MB
		LSM 880	40x oil	1.3	1.51	0.21mm	n.a	40	0.08 µm/pixel	0.54µm	Tile Scan 2x2; 3D recontruction; Maximum intensity projection	2.9 GB
	C	LSM 880	40x oil	1.3	1.51	0.21mm	n.a	40	0.08 µm/pixel	1.8µm	Tile Scan 3x3; 3D recontruction; Maximum intensity projection	3.73 GB
		LSM 880	40x oil	1.3	1.51	0.21mm	n.a	40	0.08 µm/pixel	0.95µm	Tile Scan 2x2; 3D recontruction; Maximum intensity projection	2.17 GB
Sup. Figures												
S1	A	UM II	2x; corr.-3.5	0.016	1.56	5.7mm	3.2x	6.4	0.95 µm/pixel	1.4µm	3D recontruction; Maximum intensity projection	38.2 GB
	B	UM II	2x; corr.-3.5	0.016	1.56	5.7mm	1.6x	3.2	1.95 µm/pixel	2.0µm	3D recontruction; Maximum intensity projection	56.5 GB
	C	UM II	2x; corr.-3.6	0.016	1.56	5.7mm	2x	4	1.54 µm/pixel	2.0µm	3D recontruction; Maximum intensity projection	54.2 GB
S2	A	LSM 880	20x	0.8	1.0	0.55mm	n.a	20	0.12 µm/pixel	n.a	Tile Scan 4x4; 2D single slice	641.4 MB
	B	LSM 880	20x	0.8	1.0	0.55mm	n.a	20	0.12 µm/pixel	n.a	Tile Scan 2x2; 2D single slice	160.51 MB
S3	B	LSM 780	20x	0.8	1.0	0.55mm	0.6	20x	0.69 µm/pixel	n.a	2D single slice	4226 KB
S4	A	LSM 880	20x	0.8	1.0	0.55mm	n.a	20	0.83 µm/pixel	n.a	Tile Scan 3x3; 2D single slice	18.22 MB
	B	LSM 880	20x	0.8	1.0	0.55mm	n.a	20	0.83 µm/pixel	n.a	Tile Scan 3x3; 2D single slice	18 MB
	C	LSM 880	40x oil	1.3	1.51	0.21mm	n.a	40	0.08 µm/pixel	n.a	2D single slice	26.7 MB
		LSM 880	40x oil	1.3	1.51	0.21mm	n.a	40	0.08 µm/pixel	n.a	Tile Scan 2x2; 2D single slice	106.23 MB
	D	LSM 880	40x oil	1.3	1.51	0.21mm	n.a	40	0.08 µm/pixel	n.a	Tile Scan 2x2; 2D single slice	100 MB

Legend of abbreviations

Imaging Systems

UM II	LaVision BioTec - UltraMicroscope II
LSM 880	Zeiss confocal LSM880 with Airyscan
LSM 900	Zeiss confocal LSM900
A.D. SDC	Andor Dragonfly Spinning Disk Confocal
DMi8	Leica DMi8 Inverted Fluorescent Microscope
LSM 780	Zeis confocal LSM 780
NA	Numerical aperture
RI	Refractive index
WD	Working distance
n.a.	not applicable

Objectives

2x corr.	Olympus MVPLAPO 2X/0.5; correction colar 3.5
20x	Plan-Apo 20x/0.8WD 0.55mm
20x	
DMi8	HC PL Fluotar L M25
40x	Plan-Neofluar 40x/1.3 oil WD0.21
40x	40X/0.6 LD Plan Neo

Supplementary Table 3

Antibody	Vendor	Cat #	Host	Dilution IF	Dilution WM	Stains
CD31	BD Pharmingen	550274	Rat	1/100	1/50	Pecam1, Endothelial cell
CGRP	Immunostar	24112	Rabbit	1/250	n/a	Calcitonin Gene-Related Peptide, Peptidergic sensory nerve
CytoK	Sigma-Aldrich	C2931-.2ML	Mouse IgG1	1/500	1/250	Cytokeratin, Ureteric tree
Ecad	Invitrogen	131900	Rat	1/500	1/250	E-cadherin, Tubule epithelium
Lrp2	MyBiosource	MBS690201	Mouse IgG1	1/500	1/250	Megalin, Proximal tubule
Nphs2	Invitrogen	PA579757	Rabbit	1/500	1/250	Podocin, Podocytes, Glomeruli
SMA-488	Invitrogen	53-9760-82	Mouse IgG2a	1/500	1/250	Smooth muscle actin, Arterial tree
SubP	Immunostar	20064	Rabbit	1/100	n/a	Substance P Peptidergic sensory nerve
Syn1	Invitrogen	51-5200	Rabbit	1/1000	n/a	Synapsin I, Synaptic vesicle marker
TH	Milipore Sigma	AB152	Rabbit	1/500	1/250	Tyrosine Hydroxylase Noradrenergic sympathetic nerve
Tubb3	BioLegend	801202	Mouse IgG2a	1/500	1/250	Class 3 Tubulin Pan-neuronal marker
Tubb3-594	BioLegend	801208	Mouse IgG2a	1/500	1/250	Class 3 Tubulin Pan-neuronal Marker
VAChT	SySy	139105	Guinea-Pig	1/100	n/a	Vesicular acetylcholine transporter, Parasympathetic (Cholinergic) nerve
RFP	Rockland	600901379	Chicken	1/500	1/250	Recombinant RFP (tdTomato)
Piezo2	Novus	NBP1-78624	Rabbit	1/250	n/a	Mechanosensitive sensory nerve
Piezo2	Novus	NBP1-78538	Rabbit	1/250	n/a	Mechanosensitive sensory nerve
Podxl	R&D systems	AF1658	Goat	1/500	1/250	Podocalyxin, glomeruli, endothelium